bioRxiv preprint doi: https://doi.org/10.1101/2020.06.17.156190; this version posted June 18, 2020. The copyright holder for this preprint (which was not certified by peer review) is the author/funder. All rights reserved. No reuse allowed without permission.

A general theory of coherence between brain areas

Marius Schneider[a,d], Benjamin Dann[b], Swathi Sheshadri[b,c], Hansjörg Scherberger[b,c], Martin Vinck[a,e]

[a]*Ernst Strüngmann Institute (ESI) for Neuroscience in Cooperation with Max Planck Society, Frankfurt am Main, Germany*
[b]*German Primate Center, Göttingen, Germany*
[c]*Faculty of Biology and Psychology, University of Goettingen, Germany*
[d]*International Max Planck Research School for Neural Circuits, Frankfurt am Main, Germany*
[e]*Correspondence to: martin.vinck@esi-frankfurt.de*

Abstract

What does neuronal coherence tell us about neuronal communication? Does coherence between field potentials (e.g. LFP, EEG, MEG) reflect spiking entrainment or coupling between oscillators? Is it a mechanism for communication between brain areas, or a byproduct of interareal connectivity? We hypothesized that interareal coherence is explained by the fact that outputs from one cortical area give rise to synaptic inputs in the same brain area, and correlated synaptic inputs in another area. Our mathematical analysis demonstrates that coherence between a sending and receiving area is precisely predicted from only two parameters: Interareal connectivity and oscillatory synchronization in the sending area. This model predicts narrow-band coherence even in case of a flat transfer function and in the absence of spiking entrainment in a downstream area, and reproduces frequency-specific Granger-causality patterns between brain areas (gamma feedforward, beta feedback). In general, we find that Granger-causality between field potentials is dominated by oscillatory synchronization in the sending area, whereas spiking entrainment is determined by the resonant properties of the receiver. Our model accurately reproduces LFP-LFP beta-coherence between macaque areas 7B and F5 in the absence of beta phase-locking within area F5. Together, these findings uncover a precise mechanistic model of interareal coherence as a (by)product of connectivity and power.

Keywords: Coherence; oscillation; synchronization; gamma; beta; connectomics; connectivity; entrainment; Wilson-Cowan; 7B; F5; macaque; resonance; feedforward; feedback; spike-field coherence; PPC (pairwise phase consistency); Granger-causality; LFP (Local Field Potential); EEG (Electroencephalography); ECoG (Electrocorticogram); MEG (Magnetoencephalography).

Introduction

The brain is a dynamical system that generates intelligent behavior through the interaction between different brain areas (Buzsáki, 2006; Miller and Wilson, 2008; Varela et al., 2001; Bressler, 1995; Engel et al., 2001; Singer and Gray, 1995; Nicolelis et al., 1995; Siegle et al., 2019; Fries, 2015). These interareal interactions can be studied by measuring temporal correlations (e.g. coherence, Granger-causality, cross-correlations) between electrophysiological signals from multiple brain areas. Electrophysiological signals are commonly distinguished into spike recordings and measures of population synaptic activity, for example LFP, ECoG, EEG, MEG (Nunez and Srinivasan, 2006; Pesaran et al., 2018; Buzsáki et al., 2012; Mitzdorf, 1985; Einevoll et al., 2013); we refer to the latter as "field potentials". Field potentials have obvious disadvantages as compared to spike recordings, such as: (i) The loss of spatial resolution, (ii) volume conduction, and (iii) the fact that synaptic potentials are a mixture of local and afferent inputs (Pesaran et al., 2018; Nunez and Srinivasan, 2006; Buzsáki and Schomburg, 2015; Einevoll et al., 2013; Buzsáki et al., 2012). Yet, they also have clear advantages: (i) They can be recorded non-invasively or from the cortical surface; (ii) by pooling over synaptic potentials in a large cortical volume, they can uncover weak interactions between areas.

Field potentials from different brain areas show coherent activity in various frequency bands (Buzsáki, 2006). Interareal coherence is influenced by several cognitive and behavioral factors (Grothe et al., 2012a; Gregoriou et al.,

bioRxiv preprint doi: https://doi.org/10.1101/2020.06.17.156190; this version posted June 18, 2020. The copyright holder for this preprint (which was not certified by peer review) is the author/funder. All rights reserved. No reuse allowed without permission.

2009; Salazar et al., 2012a; Richter et al., 2018; Colgin et al., 2009; Buschman and Miller, 2007; Fries, 2015; Varela et al., 2001; Babapoor-Farrokhran et al., 2017; Phillips et al., 2014; Olcese et al., 2016; Montgomery and Buzsáki, 2007; Von Stein and Sarnthein, 2000; Bressler et al., 1993; Brunet et al., 2014). Furthermore, distinct frequency bands are thought to play specific roles in interareal communication. For example, gamma (30-80Hz) and alpha/beta frequencies (10-30Hz) have been related to feedforward and feedback corticocortical communication, respectively (Buschman and Miller, 2007; Bastos et al., 2015; van Kerkoerle et al., 2014; Richter et al., 2018; Bressler et al., 2006; Mejias et al., 2016). Yet, the unequivocal functional significance and causal interpretation of these findings remains to be established. Does interareal coherence itself have an influence on the communication between areas? Or is interareal coherence a byproduct of connectivity, and hence communication, between areas (coherence through communication)?

The interpretation of interareal coherence between field potentials is fraught with many problems (Pesaran et al., 2018; Buzsáki and Schomburg, 2015; Nolte et al., 2004; Nunez and Srinivasan, 2006; Einevoll et al., 2013; Vinck et al., 2015, 2010). A well-known problem is the spread of electromagnetic fields over space (volume conduction) (Sirota et al., 2008a; Nunez and Srinivasan, 2006; Pesaran et al., 2018; Vinck et al., 2016; Carmichael et al., 2019; Parabucki and Lampl, 2017). In this paper, we investigate another major problem which we refer to as the *synaptic mixing problem*: In the normal LFP range (<80Hz), field potentials primarily reflect the summed synaptic activity (transmembrane currents) in a population of neurons (Einevoll et al., 2013; Pesaran et al., 2018; Nunez and Srinivasan, 2006; Buzsáki et al., 2012). These synaptic potentials can be decomposed into two parts: (i) Synaptic inputs caused by spikes from neurons in the *same* brain area, and (ii) afferent synaptic inputs caused by spikes from neurons in *other* brain areas. Likewise, spiking activity in one brain area (A) can cause synaptic potentials in the *same* brain area (A), and highly correlated synaptic potentials in *another* brain area (B) at a delay. We refer to these effects as "synaptic mixing". As a consequence, electric signals measured in area A and area B may, in part, be delayed copies of the same underlying signal, which would trivially give rise to interareal coherence and Granger-causality (Pesaran et al., 2018; Buzsáki and Schomburg, 2015). Because the transmission of the signal in this case is not instantaneous, the synaptic mixing problem cannot be solved with techniques that address the volume conduction problem (Trongnetrpunya et al., 2016; Pesaran et al., 2018; Nolte et al., 2004; Haufe et al., 2012; Vinck et al., 2015, 2011).

Here, we develop a general theory of the way in which synaptic mixing determines interareal coherence, using mathematical analysis, simulations of neuronal populations, and analysis of interareal recordings.

Results

Beta-coherence between areas F5 and 7B

We start out with the analysis of neural data, in which two distant brain areas show clear beta-synchronization between LFP signals. Beta-synchronization is thought to be involved in motor preparation, maintenance of a cognitive state and top-down modulation (Richter et al., 2018; Buschman and Miller, 2007; Salazar et al., 2012a; Bastos et al., 2015; Engel et al., 2001; Scherberger et al., 2005). We recorded from subdivisions of the parietal (area 7B) and premotor (area F5) cortex. These brain areas are involved in tasks like the reaching and grasping of objects (Dann et al., 2016). Premotor area F5 is one of the main projection targets of area 7B; this is a strong long-range projection, as area F5 lies several cm's away from area 7B (Johnson et al., 1996; Luppino et al., 1999; Markov et al., 2014).

We recorded LFPs and spiking activity using two 32-channel flexible microelectrode arrays per area (Figure 1A). We analyzed the memory period of the task (see Methods), in which beta oscillations are most prominent. We observed a clear beta-peak (≈20 Hz) in the power spectrum of 7B LFPs (Figure 1B). To analyze how single units were synchronized with LFPs, we computed the unbiased spike-field PPC value, which is proportional to the squared spike-field coherence (Vinck et al., 2012). Consistent with the clear LFP beta-peak, single units in 7B showed significant spike-LFP phase-locking in the beta-frequency band (Figure 1C). Spike-LFP locking was close to zero for frequencies outside the beta-band (Figure 1C). We also found coherence between the two 7B electrode grids (Figure 1F,H). Thus, synaptic and spiking activity in area 7B showed clear beta-band synchronization.

Next, we examined interareal LFP-LFP and spike-LFP coherence between area 7B and area F5. We observed relatively strong and narrow-band beta-coherence between 7B and F5 LFPs (Figure 1E). This would suggest, *prima facie*, oscillatory coupling between these two brain areas. To analyze whether this coherence was due to volume conduction, we computed a measure of coherence that avoids spurious coherence due to volume conduction, namely the Weighted

bioRxiv preprint doi: https://doi.org/10.1101/2020.06.17.156190; this version posted June 18, 2020. The copyright holder for this preprint (which was not certified by peer review) is the author/funder. All rights reserved. No reuse allowed without permission.

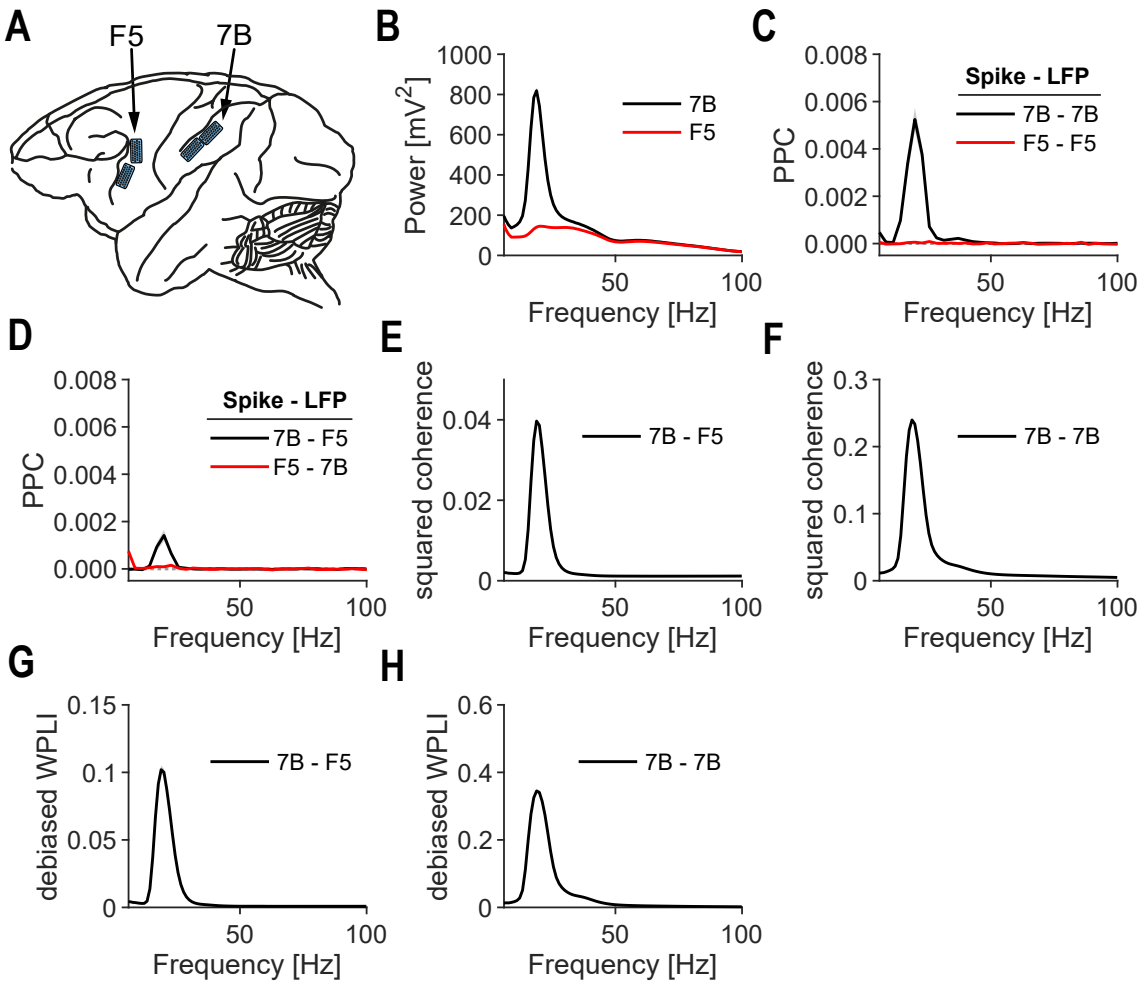

Figure 1: Coherence without spiking entrainment between macaque F5 and 7B **(A)** Illustration of electrode FMA grid recordings from the premotor areas F5 and 7B of a macaque monkey during grasping task (see Methods). We analyzed the memory period before motor execution. **(B)** LFP power spectrum for 7B (black) and F5 (red). **(C)** Spike-field phase locking (measured with PPC; see Methods) for different combinations of spikes and LFPs: Spikes in 7B to LFPs in 7B (black); spikes in F5 to LFPs in F5 (red). Phase locking values were averaged over all electrodes in corresponding grid. Spikes were pooled across all neurons in a session. The average number of neurons per session were 22.3 (7B) and 17.9 (F5). **(D)** Same as (C), but now between spikes in 7B to LFPs in F5 (black), and spikes in F5 to LFPs in 7B (red). **(E-F)** Coherence between medial and lateral 7B LFPs (F) and 7B and F5 LFPs (E). **(G-H)** Absolute value of weighted phase-lag index (Vinck et al., 2011) between 7B and F5 LFPs, as well as medial 7B and lateral 7B LFPs. The debiased WPLI is a measure of phase-synchronization robust to volume conductionn (Vinck et al., 2011). All figures have standard errors of the mean. For PPC the standard error is across 4 conditions $\times$ 6 recording sessions. For coherence and WPLI, 6 sessions were pooled for the computation, and the standard error was computed across 4 conditions.

Phase Lag Index (WPLI; see Methods) (Vinck et al., 2011). The WPLI spectrum showed beta-synchronization between 7B and F5 LFPs, suggesting that LFP-LFP coherence was not due to volume conduction (Figure 1G); this is consistent with the large spatial distance between 7B and F5.

Because there was clear beta-coherence between 7B and F5 LFPs, we expected to also find interareal beta-synchronization between spikes and LFPs. Surprisingly, we did not detect significant beta-band spike-LFP phase-locking between F5 spikes and F5 or 7B LFPs (Figure 1C-D). Moreover, we found that the LFP power spectrum in area F5 was dominated by the $1/f$ component, and showed only a small peak in the beta-band (Figure 1B). Thus, we found clear evidence for beta-oscillatory activity in area 7B and beta-coherence between F5 and 7B LFPs, but no beta-synchronization within F5. How can this discrepancy be explained?

bioRxiv preprint doi: https://doi.org/10.1101/2020.06.17.156190; this version posted June 18, 2020. The copyright holder for this preprint (which was not certified by peer review) is the author/funder. All rights reserved. No reuse allowed without permission.

Coherence predicted from connectivity and power

In this section, we will show that field-field (e.g. LFP-LFP, EEG-EEG or MEG-MEG) coherence between two brain areas ("Areas 1 and 2") can be predicted from two parameters: (i) The connection strength between Areas 1 and 2; (ii) the structure of the LFP power spectrum in both areas. We start out with the simple case of unidirectional communication, where Area-1 projects to Area-2 with a connection weight w (Figure 2A). In this case, output spikes from Area-1 can cause synaptic potentials both in Area-1 (through recurrent connections) and in Area-2 (through interareal projections). At the same time, spikes from neurons in Area-2 will also cause synaptic potentials in Area-2. Thus, the LFP in Area-2 will be a mixture of synaptic inputs from Area-1 and Area-2. We model the measured signal in Area-1 as the sum of an oscillatory process and a broad-band process, e.g. $1/f$ pink noise. We further suppose that that the intrinsic signal of Area-2 has no rhythmic (oscillatory) component. The Area-2 LFP is therefore described as a linear mixture of its own background fluctuations and the synaptic inputs from Area-1.

To understand the behavior of coherence in this model, we generated synthetic signals in both areas. A beta-oscillation in Area-1 was generated using a dampened harmonic oscillator (AR(2); see Methods). The background processes were generated as $1/f$ pink-noise signals (see Methods). As expected, Area-1 showed a clear beta-frequency peak in the power spectrum (Figure 2A). However, because of the small connection weight ($w = 0.069$), there were no visible oscillations in the power spectrum of Area-2. Moreover, the transfer function from Area-1 to Area-2 was flat, reflecting the linear superposition of inputs from Area-1 onto Area-2, and the lack of any form of filtering. Despite this flat transfer function, LFP-LFP coherence and Granger-causality between Area-1 and 2 showed a clear spectral peak in the beta frequency-band. Thus, a narrow-band peak in the coherence spectrum emerged as a byproduct of synaptic mixing.

To generalize the results of this simulation, we derived an analytical expression for the coherence spectrum based on the connection weight w and the SOS ("Sender Oscillation Strength"). The SOS was denoted α, defined as the ratio of the power spectral density of the oscillatory component, $S_{11}(f)$, relative to the background signal, $H_{11}(f)$. The squared-magnitude coherence (approximately equal to Granger-causality) between Area-1 and Area-2 equals (see Methods)

$$C^2(f) = \Theta\left(w^2\left(1+\alpha(f)\right)\right) \approx w^2\left(1+\alpha(f)\right). \tag{1}$$

Here $\Theta(x) \equiv \frac{x}{1+x}$ is a sigmoid-like function (Figure 2B). We confirm this analytical expression with numerical simulations based on generating AR(2) and $1/f$ signals (Figure 2C). This analytical expression has two main implications:

(1) Coherence and Granger-Geweke causality are monotonically increasing functions of the SOS $\alpha(f)$ and the coupling weight w. The coherence peaks at the frequency where $\alpha(f)$ reaches a maximum. Even for small values of w, coherence can show a prominent peak if $\alpha(f)$ is large. In this model, band-limited coherence between field potentials is a byproduct of communication: The coherence "itself" does not contribute to communication, because the transfer function is flat and there is no interaction between the inputs from Area-1 and the intrinsic activity of Area-2.

(2) The dependence of coherence on coupling weight has a non-linear, sigmoidal form. Hence, a change in coupling weight w causes a steep change in coherence for some values of w, but weakly affects the coherence for other values of w. Specifically, the derivative reaches a maximum for $w = 1/\sqrt{1+\alpha}$. Thus, when $\alpha(f)$ is large, steep changes in coherence already occur for relatively small coupling weights. In general, the effect of the coupling weight w on the coherence depends on the value of the SOS, $\alpha(f)$. Furthermore, a change in the coherence can be caused both by change in interareal connectivity and the SOS (Figure 2D).

Modelling the coherence between 7B and F5

We used the synaptic mixing model of coherence to reproduce the LFP-LFP coherence between areas 7B and F5. To this end, we generated beta oscillations in Area-1 (7B) as dampened harmonic oscillators, and the background processes as $1/f^n$ spectra (see Methods). This model produced an LFP-LFP coherence spectrum with a clear peak in the beta-frequency band. However, it overestimated the LFP-LFP coherence at other frequencies (Figure 2E). This suggests that our simple model of coherence cannot fully explain the interareal coherence between 7B and F5. Could there still be some "genuine" oscillatory coupling between areas 7B and F5?

bioRxiv preprint doi: https://doi.org/10.1101/2020.06.17.156190; this version posted June 18, 2020. The copyright holder for this preprint (which was not certified by peer review) is the author/funder. All rights reserved. No reuse allowed without permission.

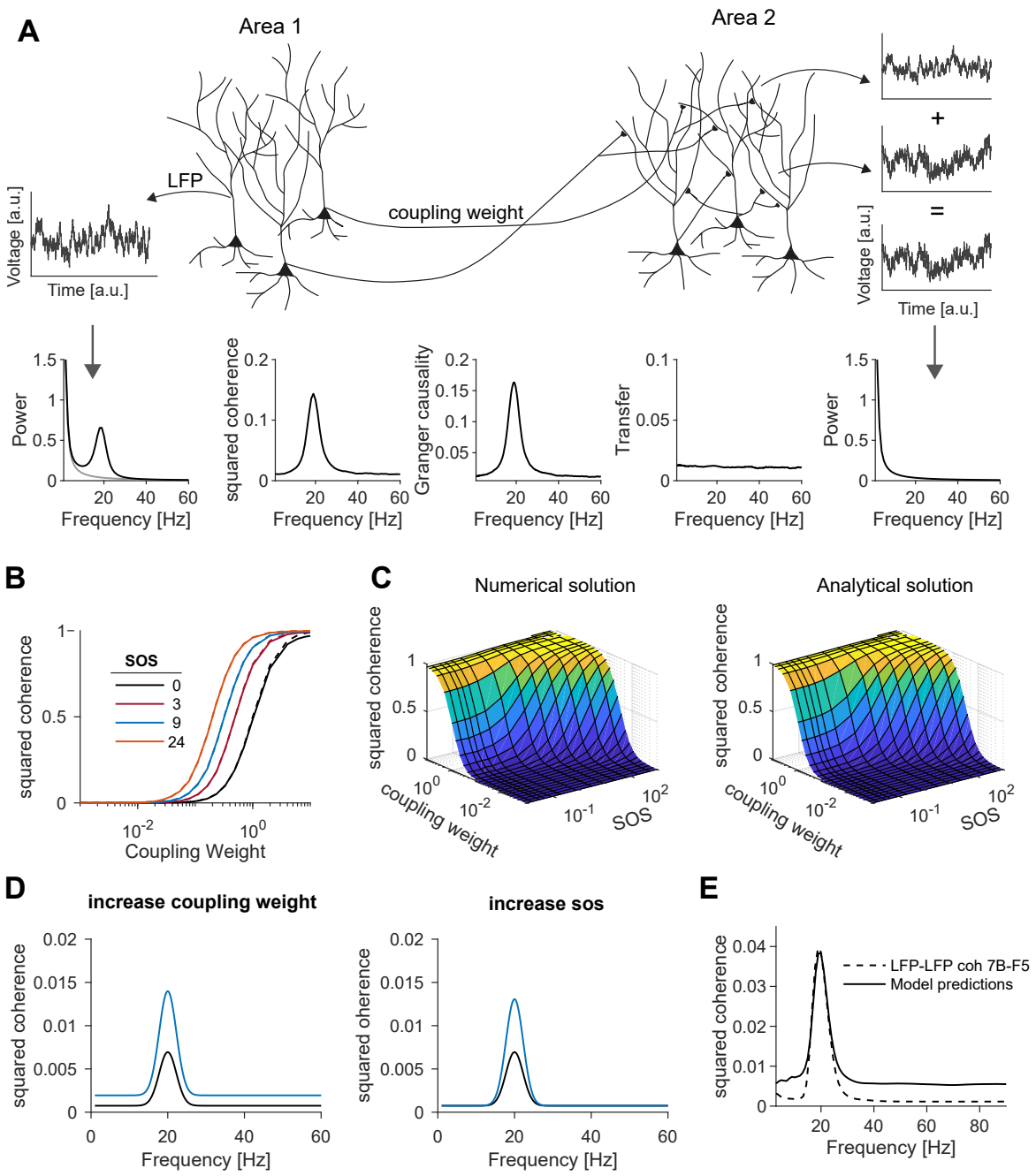

Figure 2: Interareal coherence as a (by)product of connectivity and power. **(A)** Illustration of the *synaptic mixing problem*. The Area-2 LFP is a linear superposition of intrinsic activity and afferent inputs from Area 1 weighted by w. The signal in Area-1 was modelled as a superposition of an oscillatory process and a $1/f$ background signal. The intrinsic activity in Area-2 was modelled by the same background signal. The power spectrum in Area-1 but not Area-2 shows a clear beta-peak. The coherence and Granger-causality spectra show clear beta peaks, but the transfer function is flat. The SOS (Sender Oscillation Strength) at the oscillatory frequency $f_1 = 20Hz$ was $SOS(f_1) = 14$; $w = 0.1$. **(B-C)** Coherence as a function of the SOS and coupling weight. Analytical derivation matched the numerical simulations (C), performed using autoregressive models with varying oscillation strengths. **(D)** Coherence spectra for two "behavioral" conditions, in which either the coupling weight (left) or the SOS (right) changed. The change in coherence was greater at the sender's oscillation frequency. The parameters were: $SOS = 10$ (blue and black - left), $w = 0.025$ (black - left), $w = 0.035$ (blue - left) and $SOS = 10$ (black - left), $SOS = 20$ (blue - left), $w = 0.025$. **(E)** Modelling interareal coherence between areas 7B and F5. Power spectra were fitted as a linear mixture of an AR(2) model with $1/f^n$ background fluctuations ($w = 0.069$). The coherence at the peak frequency can be well reproduced, but that the coherence at other frequencies is not fitted well.

bioRxiv preprint doi: https://doi.org/10.1101/2020.06.17.156190; this version posted June 18, 2020. The copyright holder for this preprint (which was not certified by peer review) is the author/funder. All rights reserved. No reuse allowed without permission.

The influence of the projection-source coherence

In this Section, we uncover an additional mechanism that further suppresses the coherence related to non-oscillatory background fluctuations, namely the *projection-source coherence* (Figure 3A); the influence of the projection-source coherence makes the synaptic mixing problem fundamentally different from the volume conduction problem. In the model analyzed above, the background fluctuations in the sender were projected onto the receiver *in the same way* as the oscillatory process in the sender. Specifically, the signal projected from Area-1 onto Area-2 was modelled as a fully coherent copy of the signal in Area-1. In other words, we assumed that the *inputs* into Area-2, caused by Area-1 activity, were a fully coherent copy of the total activity in Area 1. However, because of the anatomy of interareal connections, this assumption will be wrong:

The Area-1-to-2 projections will originate from a relatively small subset of neurons in Area-1, because some neurons only project to other brain areas, and some neurons project only locally (Markov et al., 2011, 2014; Han et al., 2018; Lur et al., 2016). Because the inputs into Area-2 are only caused by a *subset* of neurons in Area-1, the inputs into Area-2 will be only be partially correlated with the *total* activity in Area-1. In other words, the coherence between the summed activity of the Area-1-to-Area-2 projection neurons and the Area-1 LFP may not be equal to 1. We refer to this as the *projection-source coherence*. We will show that this coherence is an increasing function of two factors: (i) The fraction of projecting neurons. (ii) The spike-LFP coherence of the Area-1-to-Area-2 projecting neurons with the Area-1 LFP. In general, we expect that oscillations substantially enhance the spike-field coherence of individual neurons (Onorato et al., 2020; Sirota et al., 2008b; Vinck et al., 2016; Buffalo et al., 2011; Chalk et al., 2010; Buzsáki and Schomburg, 2015; Gregoriou et al., 2009) A related point, is that the projecting area typically consists of spatially separated populations of projecting neurons. The outputs of these different populations may converge onto a single receiver. In the absence of coherent activity, the LFP tends to be highly local, spanning a small cortical volume ($\approx 200\mu$m) (Lindén et al., 2011; Einevoll et al., 2013; Katzner et al., 2009). In such a volume, the total number of neurons will be only around $160000/125 = 1280$ neurons (for a density of 160000 neurons/mm^3) (Christensen et al., 2007). Out of these 1280 neurons, only few to tens of active neurons might be projecting to another given brain area. However, the coherence across populations can be strongly enhanced by rhythmic synchronization (Figure 1) (Buzsáki, 2006; Gray et al., 1989). This effectively increases the number of coherently firing projection neurons, and the spatial reach of the LFP (Lindén et al., 2011).

In the Methods section, we derive a general expression for the coherence between Area-1 and Area-2, which contains an additional dependence on the projection-source coherence, denoted $C_{\text{proj,source}}(f)$:

$$C^2(f) \approx w^2\,(\alpha(f)+1)\,C^2_{\text{proj,source}}(f)\,. \tag{2}$$

Here $\alpha(f)$ is the ratio of intrinsic power in the sender over intrinsic power in the receiver. This equation states that the original influence of the SOS and w on coherence is multiplied by the projection-source coherence. Thus, oscillations in the sender increase the interareal coherence because of two factors, $C_{\text{proj,source}}(f)$ and $\alpha(f)$.

Next, we derive an expression for the projection-source coherence $C_{\text{proj,source}}(f)$ (see Methods) as

$$C^2_{\text{proj,source}} \approx N_p\,\phi^2(f)\ . \tag{3}$$

Here, $\phi^2(f)$ is the squared spike-LFP coherence of an individual projecting neuron with the Area-1 LFP. The variable N_p represents the number of Area-1-to-Area-2 projecting neurons. By combining all equations we state our main analytical result, namely that

$$C^2 \approx w^2\,(\alpha+1)\ N_p\,\phi^2(f). \tag{4}$$

Note that the same equation applies to the coherence between Area-1-LFP and Area-2 spiking, if Area-2 spiking relates in a linear or sigmoidal way to synaptic inputs (see Methods). In sum, LFP-LFP coherence is determined by the following four factors:

1. The connection weight w *relative* to other inputs into the receiver.
2. The number of active projecting neurons in Area-1.
3. The spike-field coherence of projection neurons. From neural recordings, the value $\phi^2(f)$ can be estimated using the unbiased spike-field PPC, which approximates the spike-field coherence (Vinck et al., 2012; Onorato et al., 2020; Vinck et al., 2016).

bioRxiv preprint doi: https://doi.org/10.1101/2020.06.17.156190; this version posted June 18, 2020. The copyright holder for this preprint (which was not certified by peer review) is the author/funder. All rights reserved. No reuse allowed without permission.

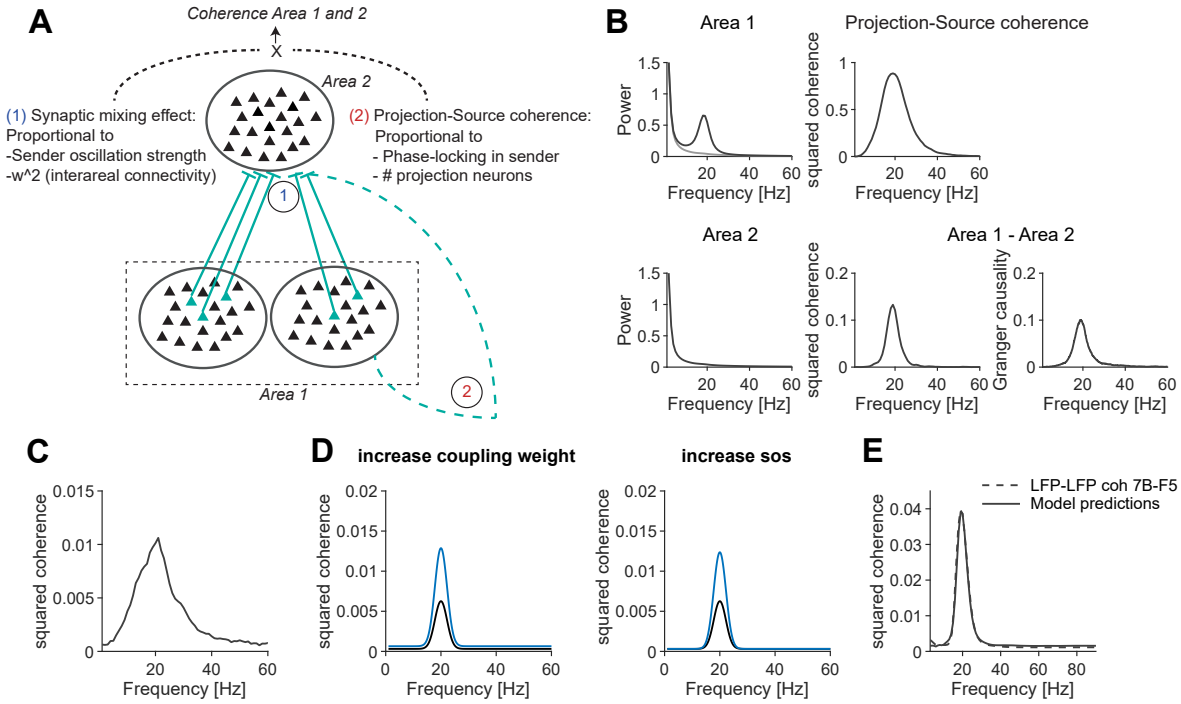

Figure 3: Interareal coherence is strongest at the frequency where the sender exhibits oscillatory synchronization. **(A)** Illustration of two mechanisms due to which coherence is suppressed at frequencies where the sender does not exhibit synchronization. The sending area consists out of multiple local sub-populations, whose projections may converge onto another area. We expect the high coherence at the oscillatory frequency, but low coherence for the background $1/f$ fluctuations. In addition, the sending area contains only a small population of Area-1-to-2 projecting neurons. The summed potential of these projecting neurons will be mostly coherent with the Area-1 LFP at the oscillation frequency. **(B)** Simulation where the subset of Area-1-to-2 projecting neurons is most coherent with the Area-1 LFP at the oscillation frequency (Top, right). The interareal coherence and Granger-causality (Bottom) show spectral peaks only at the oscillation frequency. In this case, the SOS at the oscillatory frequency was $SOS = 14$ and coupling weight $w = 0.1$; the oscillation was modelled as an AR(2). The background fluctuations in Area-1 were only partially transmitted, with a weight of $\sqrt{1-\gamma}$, $\gamma = 1$ (see Methods). **(C)** Same as in Figure (B), but now with the presence of an oscillation in Area-2 with the same strength as Area-1. In this case the coherence is substantially lower than in (B), because the SOS equals 1 for all frequencies. However, it still exhibits a spectral peak because of the coherence of the Area-1 LFP with the Area-1-to-2 projection neurons. **(D)** Both increases in coupling weight and SOS cause a narrow-band increase in interareal coherence. The parameters were: $SOS = 10$ (blue and black - left), $w = 0.025$ (black - left), $w = 0.036$ (blue - left) and $SOS = 10$ (black - right), $SOS = 20$ (blue - right), $w = 0.025$. **(E)** LFP-LFP coherence between macaque 7B and F5 (dashed) can be reproduced (solid) by the synaptic mixing model shown in (B). The background fluctuations in Area-1 are only partially transmitted, with a weight of $\sqrt{1-\gamma}$, $\gamma = 0.95$, $w = 0.077$.

4. The sender-oscillation-strength $\alpha(f)$.

We further observe that the SOS and the spike-LFP PPC are proportional to each other, i.e. $\alpha(f) \propto \phi^2(f)$ (see Methods). For small values of N_p, $\alpha(f)$ also depends linearly on N_p (see Methods). Moreover, the number of projecting neurons in an area should be proportional to the connection weight w between the areas (Markov et al., 2011, 2014). Hence we obtain the supra-linear relationship

$$C^2(f) \propto w^4 \, \phi^4(f) \tag{5}$$

for small values of w and ϕ. Hence, 2-fold changes in spike-LFP coherence or firing rates in the sending area can, *ceteris paribus*, cause a 16-fold change in the squared interareal coherence. For larger values of w and ϕ, the expression takes the linear form $C^2(f) \propto w^2 \, \phi^2(f)$ as $C_{\text{proj,source}}$ is bound by 1.

The connection weight w depends on several factors: (i) The number of synaptic connections that are made into another area; (ii) factors modulating synaptic efficacy, like compartementalized dendritic inhibition and neuromodulators (Batista-Brito et al., 2018; McGinley et al., 2015; Chiu et al., 2013).; (iii) the termination zone of the synapses, given that synaptic currents on basal and apical dendrites cancel each other out (Lindén et al., 2011); (iv) the average firing rates of the projecting neurons.

bioRxiv preprint doi: https://doi.org/10.1101/2020.06.17.156190; this version posted June 18, 2020. The copyright holder for this preprint (which was not certified by peer review) is the author/funder. All rights reserved. No reuse allowed without permission.

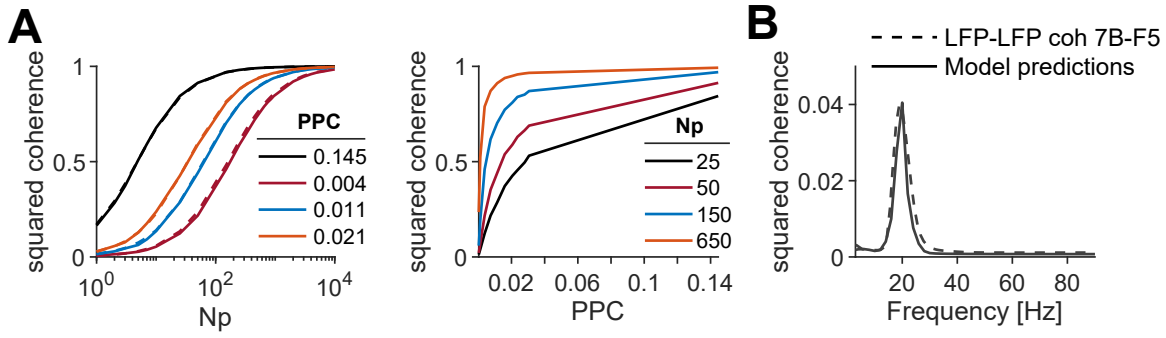

Figure 4: Analytical derivation of projection-source coherence, and interareal coherence predicted through spike-LFP Phase Locking in sender area **(A)** Squared coherence between Area-1 LFP and the summed activity of Area-1-to-2 projection neurons, as a function of the number of projecting neurons (Np) and the phase-locking of individual neurons (spike-field PPC). For this simulation, we generated an AR(2) signal in the sender and generated spikes in 10000 neurons according to inhomogenous Poisson processes modulated by this AR(2) process (see Methods). The dashed lines show a tight match between our analytical derivations and the simulations (see Methods). **(B)** Interareal coherence spectrum between 7B and F5. Data: dashes. Model: solid. Model predictions were inferred from: the spike-LFP PPC within area 7B; the SOS $\alpha(f)$; and the coupling weight w of the model in Figure 2 (E). The total number of Neurons in area 7B is 100000 (which was arbitrarily chosen) and 550 of these are projecting to area F5.

Given the dependence of interareal coherence on so many factors, it is highly non-trivial to infer changes in interareal synaptic gain as a function of cognition or behavior. To make matters worse, controlling for the average firing rate or spike-field coherence will be insufficient, because projection neurons are a highly specialized subclass of cells (Lur et al., 2016; Han et al., 2018).

Simulations of extended model

We performed several simulations to validate our theoretical model. The projection-source coherence can be incorporated by simulating the activity in the sender as a weighted superposition of two $1/f$ background processes (see Methods) (Figure 3B): The projected $1/f$ background had a weight of $\sqrt{0.05}$, and the non-projected background a weight of $\sqrt{0.95}$. In this case, the projection-source coherence equals 0.25 for the $1/f$ background process. We found that, as expected, the coherence was strongly suppressed at frequencies outside the oscillation frequency band.

An important consequence of the analytical expression in Eq. 2 is that a peak in the coherence spectrum can emerge even when the sender and receiving area have identical oscillation strength, and are not phase-synchronized. By contrast, the simple synaptic-mixing model would not predict a peak in the coherence spectrum, because $\alpha(f)$ is now equal to 1 for all frequencies. However, due to the dependence of the interareal coherence on the projection-source coherence, the coherence does attain a narrow-band structure (Figure 3C). Changes in coherence with the SOS $\alpha(f)$ or interareal connectivity w also occurred in a narrow frequency range, and were only visible at the oscillation frequency of the sender (Figure 3D).

Finally, we performed additional simulations to confirm the analytical expression obtained for the projection-source coherence (Eq. 3, 33, 39) (Figure 4A).

Explaining coherence between areas 7B and F5

We found that the coherence spectrum between 7B and F5 LFPs could not be accurately reproduced based on the SOS and interareal connectivity alone. We therefore applied the extended model, in which the $1/f$ background is only partially transmitted. The extended model was able to accurately reproduce the observed LFP-LFP coherence between 7B and F5 (Figure 3E). We further modelled the interareal coherence based on the spike-LFP PPC within area 7B (Figure 4B). For this, we used the analytical expression for the coherence based on spike-LFP PPC, the SOS $\alpha(f)$, coupling weight w and the number of projecting neurons N_p. The coherence was well predicted from this model: The required number of projecting neurons to reproduce the coherence was about 550. Note that the literature reports about two orders of magnitude more 7B-to-F5 projection neurons for a given retrograde injection in F5 (Markov et al., 2011, 2014). Together, these data suggest that beta coherence between F5 and 7B LFPs can be explained by the synaptic mixing model.

bioRxiv preprint doi: https://doi.org/10.1101/2020.06.17.156190; this version posted June 18, 2020. The copyright holder for this preprint (which was not certified by peer review) is the author/funder. All rights reserved. No reuse allowed without permission.

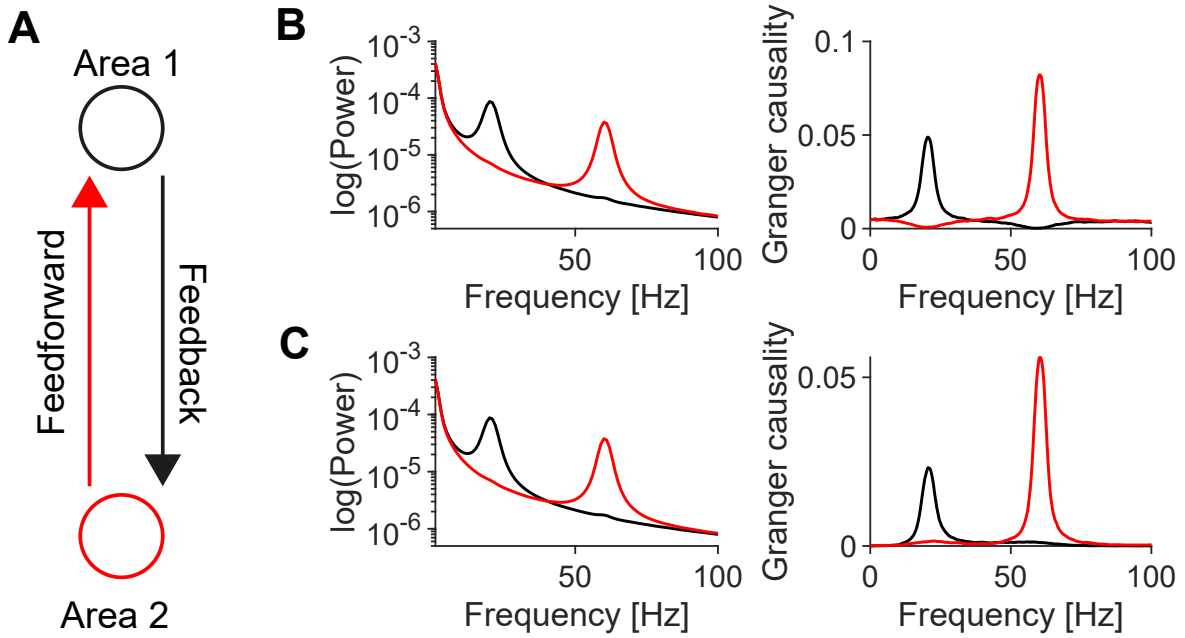

Figure 5: Gamma bottom-up and beta top-down Granger-causality are byproducts of connectivity and differences in power spectra. **(A)** We model feedforward (bottom-up) and feedback (top-down) interactions between two areas. The intrinsic activity of each area is modelled as a linear mixture of an AR(2) model and $1/f^n$ background fluctuations. The AR(2) model of Area-1 is oscillating at 20 Hz. The AR(2) model of Area-2 is oscillating at 60 Hz. The signals are transmitted to the other area with a conduction delay of 5ms. **(B)** We simulate the interareal interactions according to the simple linear synaptic mixing model shown in Figure 2. Shown from left to right are: Power spectra of Area-1 and 2 and Granger-causality in feedforward (red) and feedback (black) direction. Thus, feedforward Granger at gamma and feedback Granger at beta frequencies can be reproduced by synaptic mixing alone, but some distortions are observed for feedback gamma and feedforward beta. **(C)** Same as (B), but now for the model where the background fluctuations in Area-1 are only partially transmitted, with a weight of $\sqrt{1-\gamma}$, $\gamma = 0.95$. This again gives rise to gamma feedforward and beta feedback, but flattens the Granger-causality spectrum at frequencies outside the oscillation bands, producing a better fit to the published literature (Bastos et al., 2015). In (B) and (C) the signals were transmitted with a weight of $w = 0.08$.

Explaining frequency-dependent interactions (gamma bottom-up, beta top-down)

In the models above, we considered a unidirectional communication setting. In reality, brain areas are typically bidirectionally connected (Markov et al., 2011). The extent to which activity in Area-1 predicts activity in Area-2, and vice versa, can be quantified using Granger-Geweke-causality (Geweke, 1982). Previous studies in primate visual and parietal areas have suggested that *feedforward* and *feedback* Granger-causality are respectively strong at gamma and alpha/beta frequencies (Bastos et al., 2015; van Kerkoerle et al., 2014; Buschman and Miller, 2007; Mejias et al., 2016; Michalareas et al., 2016). One possible interpretation of these findings is that brain areas communicate with different frequencies in the feedforward or feedback direction (Bastos et al., 2015). Alternatively, frequency-specific Granger-causality might be a consequence of the presence of distinct oscillation bands in different brain areas, not of frequency-specific transfer functions. In particular, there exists a gradient of oscillation frequencies and time constants across the cortical hierarchy; gamma and beta oscillations are prominent in early visual areas and parietal cortex, respectively (see also Figure 1B) (Figure 5) (Bastos et al., 2015; Brovelli et al., 2004; Bosman et al., 2012; Vinck et al., 2016; Salazar et al., 2012a; Murray et al., 2014; Onorato et al., 2020; Spyropoulos et al., 2020; Scherberger et al., 2005).

We modelled the intrinsic signals in both Area-1 and Area-2 as the sum of a broad-band process (pink noise), and an oscillatory signal (Area-1: gamma; Area-2: beta) (Figure 5A). We then coupled the areas bidirectionally. Our synaptic mixing models accurately reproduced the Granger spectra previously reported, with stronger feedforward and feedback Granger-causality at gamma and beta frequencies, respectively (Figure 5B-C).

bioRxiv preprint doi: https://doi.org/10.1101/2020.06.17.156190; this version posted June 18, 2020. The copyright holder for this preprint (which was not certified by peer review) is the author/funder. All rights reserved. No reuse allowed without permission.

E/I networks

We found that narrow-band LFP-LFP coherence results from synaptic mixing alone. However, it is possible that oscillatory synaptic inputs cause some spiking entrainment in the receiver, which could further increase LFP-LFP coherence. Note that with "spiking entrainment", we simply mean that some spikes in the receiver are caused by the sender, not that the entire intrinsic oscillation in a receiver is phase-locked to the oscillation in a sender. To investigate this question, we modelled each area as a network of E/I neurons whose dynamics are governed by stochastic Wilson-Cowan equations. These networks show noisy oscillations that mimick oscillatory behavior in the brain (Spyropoulos et al., 2020; Wallace et al., 2011; Powanwe and Longtin, 2019; Mejias et al., 2016). Note that the E/I network did not contain dendritic low-pass filtering, which would in practice diminish the influence of excitatory to excitatory connections at higher frequencies (Buzsáki and Schomburg, 2015; Pike et al., 2000). We constructed two types of scenarios: *Mixing without entrainment:* In Simulation 1, spikes from Area-1 generated field potentials in Area-2, but the neurons in Area-2 were "blind" to the inputs from Area-2. Thus, there was synaptic mixing, but no spiking entrainment, and LFP-LFP coherence was strictly due to synaptic mixing. *Mixing with entrainment:* In Simulation 2, there was spiking entrainment, i.e. spiking in the receiver was modulated by synaptic inputs from the sender. We simulated different cases, e.g. gamma oscillations in the sender, beta oscillations in the receiver, or a combination of these. In Figure 6, we only show coherence, because Granger-causality is approximately equal to the squared coherence for unidirectional communication (see Methods).

Without spiking entrainment, we found strong LFP-LFP coherence at the frequency of the sender (Figure 6B-C), as predicted from the results obtained above. However, spiking entrainment in the receiver did not substantially contribute to the interareal LFP-LFP coherence if the sender and the receiver had different oscillation frequencies (Figure 6B-C,E).

In Figure 6D, we considered a scenario where the sender and the receiver had the same oscillation frequency (gamma) and power. Without spiking entrainment, we found only weak gamma LFP-LFP coherence 6D. This is due to the fact that the SOS was now matched to the receiver oscillation strength, i.e., $\alpha(f) = 1$ for all f (see also Figure 3). With spiking entrainment, we observed a strong increase in LFP-LFP gamma coherence. For low interareal connectivity, LFP-LFP coherence now mostly reflected spiking entrainment (Figure 6E), in contrast to the case where the receiver oscillated in a different frequency band (Figure 6B,E); this difference reflects the resonant properties of the receiver. Although LFP-LFP coherence was now more strongly influenced by spiking entrainment, the value of LFP-LFP coherence was comparable to the case where the receiver oscillated in the beta band (Figure 6E). Overall, the contribution of spiking entrainment to LFP-LFP coherence increased as the difference in oscillation frequency between sender and receiver became smaller (Figure 6G).

For all cases of sender-receiver frequencies, LFP-LFP coherence showed the stereotypical sigmoidal increase as a function of interareal connection strength. For the gamma-to-gamma simulation, spike-field phase-locking to the sender oscillations was initially weak; this indicated that most spikes in the receiver were triggered by its own intrinsic oscillations, but some spikes were triggered by the afferent oscillatory inputs (Figure 6F). With an increase in interareal connectivity, we observed a gradual increase in spike-field phase-locking (Figure 6F). Thus, there was no sudden phase transition where the intrinsic oscillations in the receiver were fully phase-locked to the sender.

These findings show that communication between a sender and receiver can produce LFP-LFP coherence in two ways: (i) By synaptic mixing, and (ii) by triggering spikes in receiver. In both cases, the amount of coherence showed a similar sigmoidal dependence on the interareal connectivity; the strength of interareal coherence was determined by interareal connectivity strength. Interareal LFP coherence should in both cases also depend on the projection-source coherence and the factors that govern it. Finally, the frequency at which spiking entrainment, i.e. actual communication, will be prominent, is determined by the resonant properties of the receiver, not the sender (Figure 7). However, the frequency at which LFP-LFP coherence or Granger-causality will be large is determined by the oscillatory properties of the sender, not the receiver.

Discussion

We showed that interareal coherence between a sending and receiving area depends on four factors: (i) The spike-field coherence of projection neurons in the sender. (ii) The oscillation strength in the sender relative to the intrinsic activity in the receiver. (iii) The interareal connectivity. (iv) The number of projection neurons. We concluded that

bioRxiv preprint doi: https://doi.org/10.1101/2020.06.17.156190; this version posted June 18, 2020. The copyright holder for this preprint (which was not certified by peer review) is the author/funder. All rights reserved. No reuse allowed without permission.

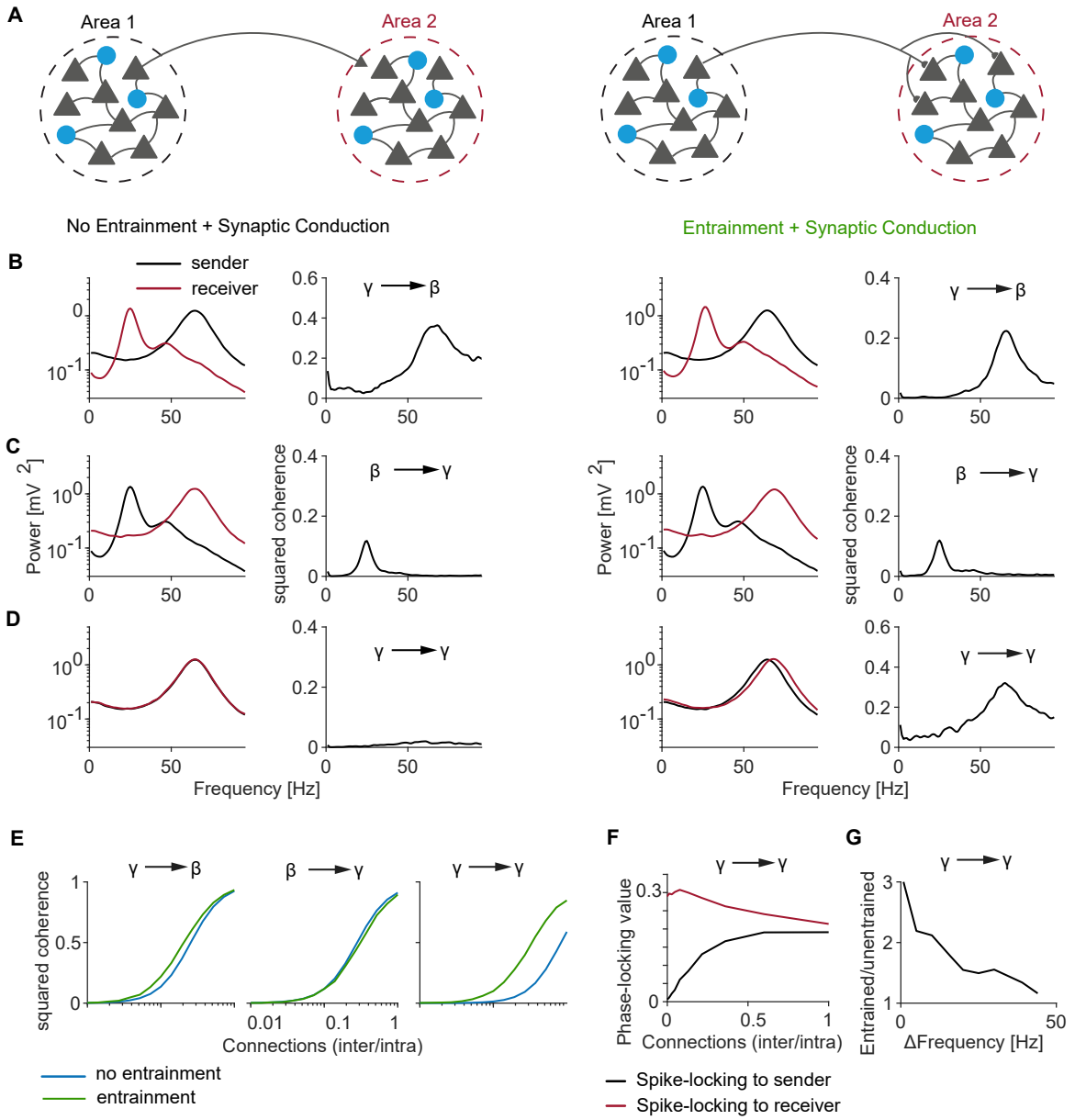

Figure 6: Spiking entrainment in the receiver does not substantially contribute to interareal LFP-LFP coherence, except when the frequencies in the sender and receiver overlap. **(A)** Illustration of the two models. Each area consisted of a population of spiking neurons whose dynamics were modelled by stochastic Wilson-Cowan equations. In the first model (left two columns), synaptic potentials due to inputs from Area-1 were superimposed onto the synaptic potentials from Area-2 itself. Neurons in Area-2 were "blind" to the synaptic inputs from Area-1, i.e. spiking entrainment was prohibited. The second model (right two columns) is identical to the first model, however synaptic inputs from Area-1 could now entrain the neurons in Area-2. **(B)** First two columns: Sender oscillates at gamma and the receiver at beta. Coherence spectra show clear peaks, following the power in the sender. Last two columns: Spiking entrainment increases coherence slightly. **(C)** and **(D)** Same as in (B), but now with different oscillation frequencies. When the oscillation frequency in the sender matches with the receiver, there is a increase in LFP-LFP coherence due to spiking (D). (B-D) all for coupling value of $w = 0.1$. **(E)** Change in coherence as a function of the ratio of inter- to intra-regional connection rates. **(F)** Spike-field phase-locking-value of neurons in the receiver population to the oscillations in the receiver (i.e. sum of all synaptic inputs caused by spikes in Area 2) and oscillations in the sender (i.e. sum of all synaptic inputs caused by spikes in Area 1). As the number of connections increases, the phase locking gradually increases. **(G)** Change in coherence going from unentrained to entrained case, expressed as a ratio, for $w = 0.05$. A value of 3 means 3 times more coherence in the entrained than the unentrained case.

bioRxiv preprint doi: https://doi.org/10.1101/2020.06.17.156190; this version posted June 18, 2020. The copyright holder for this preprint (which was not certified by peer review) is the author/funder. All rights reserved. No reuse allowed without permission.

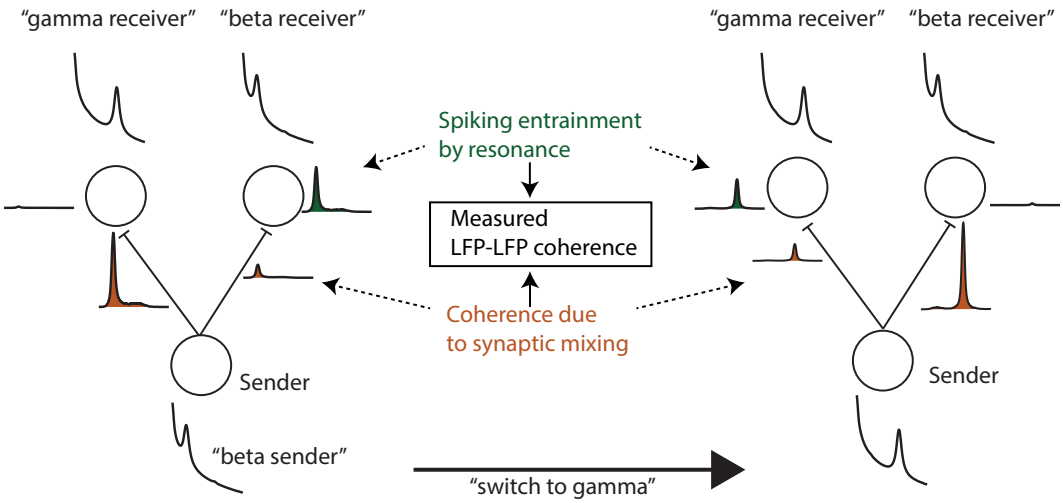

Figure 7: Illustration of difference between LFP-LFP coherence and spiking entrainment, and ability to switch communication by changing oscillations in the sender. In the left case, the sender oscillates at beta, and it would have a high LFP-LFP coherence with a receiver at gamma due to synaptic mixing. However, this LFP coherence does not translate into spiking entrainment. When the receiver also oscillates at beta, the LFP coherence due to synaptic mixing is lower, but due to resonance, the receiver will now exhibit more spiking entrainment. In the right case, the sender switches to gamma, and now switches communication to the gamma receiver. Paradoxically, LFP-LFP coherence might be higher between the sender and the receiver that communicate less.

narrow-band coherence between field potentials is a predicted byproduct of power and connectivity: It does not require coupling between oscillators, frequency-specific information transmission, or spiking entrainment.

Dynamic changes in interareal coherence with cognition can be caused by a combination of these four factors, including the interareal connectivity. Although the anatomical substrate of interareal connectivity changes slowly, interareal connectivity can be rapidly modulated by several mechanisms. These include (i) compartmentalized dendritic inhibition and (ii) neuromodulators (Batista-Brito et al., 2018; McGinley et al., 2015; Chiu et al., 2013). Gain modulation of firing rates in the sending area also leads to an effective increase in interareal connectivity, if the firing rates of other sources of synaptic input do not change. We conclude that band-limited changes in interareal LFP-LFP coherence do not imply frequency-specific changes in information transmission. In fact, a change in interareal connectivity is expected to increase information transfer at *all* frequencies. However, at the level of LFP-LFP coherence, a change in e.g. interareal connectivity only has *measurable* effects at the frequencies where neurons in the sending area fire synchronously (Figure 3).

A function for coherence?

There are numerous theories ascribing functional roles to interareal phase-synchronization and coherence in coordinating neuronal interactions, e.g. (Varela et al., 2001; Bressler, 1995; Engel et al., 2001; Kreiter, 2006; Fries, 2005; Miller and Wilson, 2008; Abeles, 1982; Bonnefond et al., 2017; Salinas and Sejnowski, 2001; Singer and Gray, 1995; Palmigiano et al., 2017; Börgers and Kopell, 2008; Buzsáki and Draguhn, 2004; Vinck et al., 2013a). Various aspects of these theories have been summarized in the CTC ("communication-through-coherence") hypothesis (Fries, 2005, 2009, 2015), which contains three premises: (i) Interareal coherence reflects phase synchronization between the *intrinsic* oscillations in the sender and receiver. (ii) Interareal communication is enhanced when afferent synaptic inputs consistently arrive at an excitable phase of the intrinsic oscillation (Volgushev et al., 1998; Burchell et al., 1998). (iii) Selective communication is implemented through selective coherence (Fries, 2015).

The current paper takes a very different point of view: Two brain areas can only communicate if they are connected, and if they are connected, they will exhibit coherence at a "good" phase-relationship. This is due to the fact that the sending area will be coherent with the inputs that the sender causes in the receiving area. The resulting coherence

bioRxiv preprint doi: https://doi.org/10.1101/2020.06.17.156190; this version posted June 18, 2020. The copyright holder for this preprint (which was not certified by peer review) is the author/funder. All rights reserved. No reuse allowed without permission.

is a consequence of communication, not a cause of it. To demonstrate coherence between *intrinsic oscillations*, it is therefore imperative to rule out that interareal coherence is not due to synaptic mixing. Otherwise, the cause (connectivity and communication) can be easily confused with the effect (coherence). And, if coherence is byproduct of communication, then it is unclear what experimental outcomes would possibly falsify CTC; if cognition is expected to increase interareal communication, e.g. due to attention, then an increase in coherence would *a priori* be an expected outcome.

Theories like CTC also propose that communication between two connected areas can be blocked by the absence of coherence (Fries, 2009): Yet, synaptic mixing models also predict that there is no coherence if there is no communication. Furthermore, communication is not consistently blocked by the absence of coherence, because interareal phase-relationships randomly fluctuate between "good" and "bad" phases (Akam and Kullmann, 2012). Alternatively, interareal communication may be prohibited by interareal coherence with a consistent "bad" phase-relationship (Volgushev et al., 1998; Burchell et al., 1998; Fries, 2005; Tiesinga and Sejnowski, 2010; Akam and Kullmann, 2012). This could block communication quite effectively (Volgushev et al., 1998; Burchell et al., 1998; Tiesinga and Sejnowski, 2010; Akam and Kullmann, 2012) and is not predicted by synaptic mixing models; however, phase separation between competing inputs has not been reported in studies that examined the modulation of interareal coherence by attention (Grothe et al., 2012a; Bosman et al., 2012).

How do we disentangle coherence through communication from phase-synchronization between intrinsic oscillations? The strength of interareal coherence may be one indicator as to whether coherence can be explained by synaptic mixing. Because interareal connections are typically weak (Markov et al., 2014, 2011), synaptic mixing is unlikely to yield very high coherence values; these would be more indicative of a pacemaker or strong coupling between oscillators. However, the most compelling correlational evidence for CTC is a moderate change in V1-V4 gamma-coherence with attention (from about 0.06 to 0.09, i.e. squared-magnitude coherence values below 0.01) (Ferro et al., 2020; Bosman et al., 2012; Grothe et al., 2012b). Notably, area V1 contains a very strong source of narrow-band gamma, which is associated with a unique class of excitatory neurons (Gray and McCormick, 1996; Onorato et al., 2020) and shows up to 300-fold power increases (Spyropoulos et al., 2020)). Thus, it should be easy to induce weak V1-V4 gamma coherence and feedforward Granger with synaptic mixing models (see Figure 5). A local increase in the firing rates and phase-locking of V1 or V2 projection neurons with attention would then be sufficient to increase V1-V4 coherence, even in the absence of coupling between local V1 and V4 oscillators (Luck et al., 1997; van Kerkoerle et al., 2014; Buffalo et al., 2011; Chalk et al., 2010).

These considerations highlight a basic problem, namely how to experimentally identify *intrinsic* oscillations using "local" field potential signals, which contain a mixture of local and afferent synaptic inputs (Buzsáki and Schomburg, 2015; Pesaran et al., 2018; Saleem et al., 2017). The strength and prevalence of oscillations show great variation across the cortical sheet; distinct brain regions have particular spectral profiles (Buzsáki, 2006). A few brain regions exhibit very strong oscillations under specific sensory or behavioral conditions. For example: there is a strong source of gamma in V1/V2 (Gray et al., 1989; Peter et al., 2019; Vinck and Bosman, 2016; Onorato et al., 2020; Henrie and Shapley, 2005; Spyropoulos et al., 2020); beta in parieto-frontal cortex (Figure 1,(Scherberger et al., 2005; Dann et al., 2016; Brovelli et al., 2004; Salazar et al., 2012b; Hagan et al., 2012; Donoghue et al., 1998; Murthy and Fetz, 1996)); and theta and gamma in rodent hippocampus (Buzsáki, 2006; Colgin et al., 2009; Bragin et al., 1995). Coherence between these oscillatory sources and areas with weak or no intrinsic oscillations will be dominated by synaptic mixing (Figure 1, (Schomburg et al., 2014)); due to synaptic mixing, oscillations will now appear in areas without intrinsic oscillations. The contribution of afferent inputs to the LFP might depend strongly on the cortical layer. Feedforward projections target the granular layer 4, which has relatively little recurrent connectivity (Lund et al., 2003), and may not exhibit intrinsic oscillatory activity (Livingstone, 1996; Xing et al., 2012). Local field potentials in layer 4 might therefore be dominated by synaptic mixing of afferent inputs, and spiking entrainment in pyramidal neurons might be strongly diminished because of dendritic low-pass filtering (Buzsáki and Schomburg, 2015). To identify that oscillations have at least some local component, it is critical to analyze local spiking activity. However, because interareal projections may induce only weak spiking entrainment in the receiver, spiking entrainment by itself does not demonstrate intrinsic oscillations in the receiver. Suppression of brain areas can be a useful diagnostic tool: For example, (Saleem et al., 2017) showed that in mouse V1, luminance/locomotion-related LFP oscillations in the 60-65Hz range are driven by LGN afferents and not affected by pharmacological suppression of V1 spiking activity.

Even if there are clear intrinsic oscillations with overlapping frequency bands in two connected areas, it is often unclear what mechanism would make them phase-synchronized, and how to measure this. In principle, intrinsic

bioRxiv preprint doi: https://doi.org/10.1101/2020.06.17.156190; this version posted June 18, 2020. The copyright holder for this preprint (which was not certified by peer review) is the author/funder. All rights reserved. No reuse allowed without permission.

oscillations can be phase-synchronized by a pacemaker that entrains multiple areas. Clear examples are subcortical areas like the thalamus (sleep spindles) and the medial septum (hippocampal theta) (Steriade et al., 1993; Wang, 2002). Yet it is unclear whether there are pacemakers for neocortical rhythms like gamma and beta. The notion of a pacemaker becomes especially problematic for oscillations that are generated by local circuits and show substantial, stochastic fluctuations in instantaneous amplitude and frequency (e.g. V1 gamma) (Spyropoulos et al., 2020; Burns et al., 2011); in this case a pacemaker would have to continuously reset the ongoing rhythm.

Previous studies have raised other theoretical concerns about the suitability of coherence as a mechanism for selective communication: (1) How can communication be made selective when there is no intrinsic oscillatory activity? For example, V1 gamma can be found for some (e.g. large gratings) but not for other stimuli (e.g. irregular textures), even though both can be seen and attended to (Hermes et al., 2015; Vinck and Bosman, 2016; Henrie and Shapley, 2005; Peter et al., 2019; Ray and Maunsell, 2015). How does attention change interareal coherence for the latter kind of stimuli? (2) Spectral coherence can only be defined over longer time periods, and is usually computed over many trials, in contrast to instantaneous phase. For reliable, selective transmission of one out of multiple sources of afferent inputs, very strong coherence differences and a long integration window are needed (Akam and Kullmann, 2012). This holds true especially when oscillators show stochastic fluctuations in instantaneous frequency (Akam and Kullmann, 2012).

Connectivity mapping through coherence

How to move forward? The synaptic mixing problem can to some extent be addressed by analyzing the (laminar) current-source-densities instead of field potentials, and techniques like ICA (Pesaran et al., 2018; Mitzdorf, 1985; Einevoll et al., 2013; Buzsáki and Schomburg, 2015; Buzsáki et al., 2012; Schomburg et al., 2014). To interpret LFP-LFP coherence, it is also critical to analyze spike-spike and spike-field synchronization (Pesaran et al., 2018; Buzsáki and Schomburg, 2015). In general, it is not *a priori* obvious whether rhythmicity in weak afferent inputs is at all transferred to spiking outputs, and whether weak entrainment is physiologically meaningful or not. Spiking entrainment may be prevented or boosted by several various factors: (i) Non-linearities in single neurons and recurrent networks; (ii) Dendritic low-pass filtering in pyramidal neurons (Buzsáki and Schomburg, 2015; Pike et al., 2000), which counteracts spiking entrainment in the gamma-frequency range (Schomburg et al., 2014; Vinck et al., 2016; Buzsáki and Schomburg, 2015); (iii) Resonance in the receiver (Figure 6).

Even if neuronal responses are linearly or sigmoidally related to afferent synaptic inputs, spike-field coherence can still be explained as a by-product of interareal connectivity and the projection-source coherence (see Methods). For various reasons, the interareal spike-field coherence of a *single* neuron might be very weak compared to the field-field coherence (see Methods, and Figure 1). One reason is that each neuron in the receiver might be targeted by only a few projection neurons, such that it sees a noisy and distorted copy of the rhythm of the sending area (see Methods).

Despite its limitations, interareal LFP-LFP coherence remains a promising tool for studying interareal connectivity and dynamic changes therein, especially in human ECoG. For example, (Bastos et al., 2015; Michalareas et al., 2016) have shown that in the primate visuo-parietal system, interareal Granger-causality between LFP signals can predict layer-specific anatomical projection patterns. Our results suggest that interareal connectivity can be best predicted at the frequencies where one of the areas has a strong intrinsic oscillation (Figure 3 and 6). Improved estimates can be obtained based on the spike-field coherence of projecting neurons (Figure 3. Further progress can be made by factoring in "third area sources" in connectivity and coherence estimates, and the contribution of spiking entrainment. Thus, the presented theoretical model of coherence and Granger-causality opens new avenues for mapping interareal connectivity in the human brain, providing an interesting alternative to DTI.

Acknowledgements and Authorship contributions

We thank Prof. Dr. Wolf Singer, Dr. Georgios Spyropoulos, Patrick Jendritza, and Dr. Craig Richter for very helpful comments. Conceptualization: MS and MV. Mathematical analysis: MS and MV. Simulations and data analysis: MS. Macaque surgeries, recordings and data preprocessing: BD, SS and HS. Writing: MS and MV. Supervision: MV. This projected was supported by ERC Starting Grant to MV (SPATEMP) and a BMF Grant to MV (Bundesministerium fuer Bildung und Forschung, Computational Life Sciences, project BINDA, 031L0167).

bioRxiv preprint doi: https://doi.org/10.1101/2020.06.17.156190; this version posted June 18, 2020. The copyright holder for this preprint (which was not certified by peer review) is the author/funder. All rights reserved. No reuse allowed without permission.

Methods

Subjects

Neural activity was recorded simultaneously from many channels in one female rhesus macaque monkey (Animals S, body weight 9, 7 kg). Detailed experimental procedures have been described previously (Dann et al., 2016). All procedures and animal care were in accordance with German and European law and were in agreement with the Guidelines for the Care and Use of Mammals in Neuroscience and Behavioral Research (National Research Council, 2003).

Macaque data

The monkey was trained to perform a delayed grasping task. In this task, the monkey was either instructed to grasp a target with one of the two possible grip types (power and precision), or free to choose between the grip types, as described in detail in previous studies (Dann et al., 2016). During instructed trials, the monkey was visually cued by one of two discs displayed on a monitor to perform the associated grip type. During free-choice trials, both discs were displayed and monkeys could choose freely between grip type. To encourage switching behavior during consecutive free-choice trials, the reward was iteratively reducing every time the monkey repeatedly chose the same grip type. Note that also delayed instructed trials were part of the task. These were not used in this study and are therefore not further explained. The monkey learned to perform the task with high accuracy of 95 +- 0.01 % SD successful trials on average.

Surgical procedures have been described in detail previously (Dann et al., 2016). In short, the monkey was implanted with four chronically implanted 32-channel microelectrode arrays (FMAs; Microprobes for Life Sciences; 32 electrodes; spacing between electrodes: 0.4mm; length: 1.5 to 7.1 mm monotonically increasing to target grey matter along the sulcus), two in part of the ventral premotor cortex (area F5) and two in area 7B, specifically around the anterior intraparietal area (AIP), for a total of 128 channels. Electrode signals from the implanted arrays were amplified and digitally stored using a 128 channel recording system (Cerebus, Blackrock Microsystems; sampling rate 30 kS/s; 0.6-7500Hz band-pass hardware filter).

To detect spikes, electrode signals were first high-pass filtered with a median filter (window length 3ms) and then low-pass filtered with a non-causal Butterworth filter (5000 Hz; 4 th order). Next, common noise-sources were eliminated by applying principal component (PC) artifact cancellation and spike waveforms were detected and semi-automatically sorted using a modified version of the offline spike sorter Waveclus. Finally, redetection of the different average waveforms (templates) was done to detect overlaid waveforms. The exact procedures of spike detection are described previously (Dann et al., 2016). Note that only well isolated single units were used for all analyses. To detect LFPs, electrode signals were first low-pass filtered with a median filter (window length 6.7 ms) and then high-pass filtered with a non-causal Butterworth filter (1 Hz; 4th order). In order to filter outpower line noise and their harmonic and additional band-stopfilter filtering out signals between 49 and 51 Hz and 98 and 102 was applied. Subsequently, signals were down-sampled by averaging 30 consecutive frames from 30000 to 1000 Hz. Broken channels and trials containing movement noise were removed from all further data analyses. For this purpose, the total power, the correlation and the maximum deflection of all channels and trails was compared and all outliers discarded. Finally, to reduce the influence of the on array ground and reference electrode on each array, the trimmed mean over all channels per array (leaving highest two and the lowest two values per time point out) was removed by using linear regression. After spike and LFP detection, single neuron spike events were binned in non- overlapping 1-ms windows to obtain an equal sampling rate of 1000 Hz for both signals. Subsequently, signals were aligned to cue and movement onset for the instructed- and free- choice-task, since activity was locked to both events.

All analyses of macaque data were performed in Matlab (Mathworks) using custom scripts and the FieldTrip toolbox (Oostenveld et al., 2011). Power and coherence spectra were assessed using integration windows of 0.35s length moved over the whole data in steps of 50ms. The epochs were Hann tapered to avoid spectral leakage. Pairwise phase consistency (PPC) between spikes and LFPs was calculated using windows of 350ms around every spike (Vinck et al., 2012), using the spiketriggeredspectrum functions in the FieldTrip SPIKE toolbox. To compute spike-LFP PPC, we first pooled the activity of single units in the area together, which gives the most sensitive estimate of entrainment in an area by increasing the number of pairwise phase comparisons (Vinck et al., 2013b).

bioRxiv preprint doi: https://doi.org/10.1101/2020.06.17.156190; this version posted June 18, 2020. The copyright holder for this preprint (which was not certified by peer review) is the author/funder. All rights reserved. No reuse allowed without permission.

Predicting interareal coherence based on connectivity and power

In this Section we derive an analytical expression for coherence based on interareal connectivity and power.

We start out from a unidirectional communication setting, where brain Area-1 projects to brain Area-2. The measured signals are denoted $z_1(t)$ and $z_2(t)$. In the following derivations, and our simulations, we assume that the signals are measured without the addition of extrinsic noise. That is we assume that all signals reflect neural activity, and we assume that there is no volume conduction.

We model the signal $z_1(t)$ in Area-1 as the sum of an oscillatory process $s_1(t)$ and a broad-band process, e.g. Pink noise, $\eta_1(t)$:

$$z_1(t) \equiv s_1(t) + \eta_1(t)\,. \tag{6}$$

The intrinsic signal $z_2(t)$ of Area-2 has no rhythmic component and is modelled as a linear mixture of its own noise term and the projected input from Area-1,

$$z_2(t) = \eta_2(t) + w\,(s_1(t) + \eta_1(t)) \tag{7}$$

where w denotes the projection strength from Area-1 to Area-2. We assume that the background processes $\eta_1(t)$ and $\eta_2(t+\tau)$ are linearly uncorrelated for all τ. For the purpose of mathematical derivation, we suppose that the power spectral densities of the broad-band processes are equal for all f, i.e. $H_{11}(f) = H_{22}(f) \equiv H(f)$, with f frequency. We denote the spectral density of $s_1(t)$ as $S_{11}(f)$. We define the SOS ("Sender Oscillation Strength") as

$$\alpha(f) \equiv \frac{S_{11}(f)}{H_{11}(f)} \equiv \frac{S_{11}(f)}{H(f)}\,. \tag{8}$$

The cross-spectral density between $z_1(t)$ and $z_2(t)$ equals

$$\begin{aligned} Z_{12}(f) &= w\,(S_{11}(f) + H_{11}(f)) \\ &= w\,Z_{11}(f) \end{aligned} \tag{9}$$

and is real-valued. Note that the other cross-terms fell out because we assumed that η_2, η_1 and s_1 are uncorrelated. The squared coherence $C^2(f)$ between Area-1 and Area-2 is defined by

$$C^2(f) \equiv \frac{|Z_{12}(f)|^2}{Z_{11}(f)\,Z_{22}(f)}. \tag{10}$$

This simplifies as follows:

$$\begin{aligned} C^2(f) &= \frac{w^2 Z_{11}(f)^2}{Z_{11}(f)\,Z_{22}(f)} \\ &= \frac{w^2\,Z_{11}(f)}{Z_{22}(f)}\,. \end{aligned} \tag{11}$$

Since $\eta_2(t)$ and $s_1(t)$ are uncorrelated, we have

$$Z_{22}(f) = H(f) + w^2 Z_{11}(f)\,. \tag{12}$$

Eq. 8 now reduces to

$$\begin{aligned} C^2(f) &= \frac{w^2\,Z_{11}(f)}{H(f) + w^2\,Z_{11}(f)} \\ &= \frac{1}{1 + H(f)\,(w^2\,Z_{11}(f))^{-1}}\,. \end{aligned} \tag{13}$$

From Eq. 8 it follows that

$$Z_{11}(f) = H(f)\,(\alpha(f) + 1)\,. \tag{14}$$

bioRxiv preprint doi: https://doi.org/10.1101/2020.06.17.156190; this version posted June 18, 2020. The copyright holder for this preprint (which was not certified by peer review) is the author/funder. All rights reserved. No reuse allowed without permission.

Hence $H_{22}(f)\left(w^2 Z_{11}(f)\right)^{-1}$ reduces to the expression

$$\frac{1}{w^2\left(\alpha(f)+1\right)}\,. \tag{15}$$

Thus the coherence can be simplified to

$$\begin{aligned} C^2(f) &= \frac{w^2\left(1+\alpha(f)\right)}{1+w^2\left(1+\alpha(f)\right)} \\ &= \Theta\left(w^2\left(1+\alpha(f)\right)\right), \end{aligned} \tag{16}$$

where $\Theta \equiv \frac{x}{1+x}$ is the sigmoid function.

We can estimate the connectivity weight from the measurement variables by solving for w and $\alpha(f)$,

$$\begin{aligned} w &= \sqrt{\frac{C^2(f)}{-(\alpha(f)+1)(C^2(f)-1)}} \\ &\approx \sqrt{\frac{C^2(f)}{\alpha(f)+1}}\,, \end{aligned} \tag{17}$$

Here, the approximation is based on the first-order Taylor expansion of the coherence around $C(f) = 0$. We can also take the Taylor expansion around $w = 0$ for Eq. 16 and obtain

$$C^2(f) \approx w^2(1+\alpha(f))\,. \tag{18}$$

Note that the same model derivations (and the derivations below) pertain to Granger-causality, because for unidirectional coupling the following relationship holds between Geweke-Granger causality and coherence (Geweke, 1982):

$$G_{1\to 2}(f) = -\ln(1-C^2(f)) \approx C^2(f)\,, \tag{19}$$

where the approximation was made based on the first order Taylor-expansion around $C(f) = 0$.

Model of interareal coherence taking into account projection patterns

In the model above we assumed that the signal received by the receiver is fully coherent with the signal in the sender. As explained in more detail in the Results Section, this is likely not the case for two reasons: 1) The sender consists of sub-populations that are not fully coherent with each other, especially for frequencies where there is no oscillatory synchronization. 2) The number of projecting neurons in Area-1 may be small, and the coherence between the summed potential of Area-1-to-2 projection neurons and the Area-1 LFP (the projection-source coherence) may not be 1.

Expression of the coherence based on power, interareal connectivity and coherence between Area-1-to-2 projection neurons and the Area-1 LFP.

We first derive an expression of the interareal coherence that includes a linear dependence on the projection-source coherence.

We model the signals as

$$z_1(t) = s_1(t) + \eta_1(t) \tag{20}$$

$$z_2(t) = \eta_2(t) + w\left(s_1^*(t) + \epsilon_1(t)\right)\,. \tag{21}$$

Here, $s_1^*(t)$ is the projected oscillatory signal into Area-2, and $\epsilon_1(t)$ is the projected background signal into Area-2. The coherence between $\eta_1(t)$ and $\epsilon_1(t)$ is denoted $C_{\eta,\epsilon}(f)$. The coherence between $s_1(t)$ and $s_1^*(t)$ is denoted $C_{s,s}(f)$.

bioRxiv preprint doi: https://doi.org/10.1101/2020.06.17.156190; this version posted June 18, 2020. The copyright holder for this preprint (which was not certified by peer review) is the author/funder. All rights reserved. No reuse allowed without permission.

We assume that $s_1(t)$ and $s_1^*(t)$ have the same power spectral densities. Likewise we assume that $\eta_1(t)$, $\eta_2(t)$ and $\epsilon_1(t)$ have the same power spectral densities.

We now obtain

$$\begin{aligned} Z_{12}(f) &= w\left(C_{s,s}(f)\, S_{11}(f) + C_{\eta,\epsilon}(f)\,, H(f)\right) \\ &= w\left(C_{s,s}\,\alpha(f) + C_{\eta,\epsilon}(f)\right) H(f)\,; \\ Z_{11}(f) &= S_{11}(f) + H(f) \\ &= (1+\alpha(f))\, H(f)\,; \\ Z_{22}(f) &= w\, S_{11}(f) + (1+w)\, H(f) \\ &= (1 + w\,(1+\alpha(f)))\, H(f) \end{aligned} \tag{22}$$

The squared coherence $C^2(f)$ now simplifies as

$$C^2(f) \equiv \frac{w^2\left(C_{ss}(f)\,\alpha(f) + C_{\eta,\epsilon}(f)\right)^2}{(1+\alpha(f))\,(1+w\,(1+\alpha(f)))}\,. \tag{23}$$

Plugging in $\alpha(f) = 0$ for all f we obtain

$$C_{12}^2(f) = \frac{w^2\, C_{\eta,\epsilon}^2(f)}{w+1} \tag{24}$$

$$\approx w^2\, C_{\eta,\epsilon}^2(f) \tag{25}$$

where the first-order Taylor expansion was made around $w = 0$. Thus, the squared coherence between areas scales with the coupling weight and the squared interareal coherence in the sender. For the oscillatory part, assuming the background fluctuations have coherence close to zero, we have

$$C^2(f) \approx w^2 \frac{\alpha(f)^2}{\alpha(f)+1} C_{s,s}^2(f) \tag{26}$$

Following the same derivation we can also obtain an expression for the squared coherence that combines both the noise and the oscillatory term as

$$\begin{aligned} C^2(f) &\equiv \frac{w^2\left(C_{\text{proj,source}}(f)\,(\alpha(f)+1)\right)^2}{(1+\alpha(f))\,(1+w\,(1+\alpha(f)))} \\ &\approx C_{\text{proj,source}}^2\,(\alpha+1)\, w^2\,. \end{aligned} \tag{27}$$

Here $C_{\text{proj,source}}$ is the projection-source coherence, and $\alpha(f)$ is defined as the ratio of power of the intrinsic signal in the sender over the intrinsic signal in the receiver.

Expression of the coherence based on power, interareal connectivity and the projection-source coherence

We derive the projection-source coherence based on N_p active (i.e. firing spikes) projecting neurons as follows. Let $x_i(t)$ be the activity of a single neuron in Area-1 with power spectral density $X(f)$ for all i. The cross-spectral density of the N_p projecting neurons with the signal based on all N_t neurons in Area-1 equals

$$X_{\text{proj,source}}(f) = N_p X(f) + N_p\,(N_t - 1)\, X(f) c(f)\,, \tag{28}$$

where $c(f)$ is the coherence between two individual neurons,

$$c(f) \equiv \frac{X_{i,j}(f)}{X(f)}\,. \tag{29}$$

bioRxiv preprint doi: https://doi.org/10.1101/2020.06.17.156190; this version posted June 18, 2020. The copyright holder for this preprint (which was not certified by peer review) is the author/funder. All rights reserved. No reuse allowed without permission.

The factor $(N_t - 1)$ accounts for the fact that each projecting neuron is fully coherent with itself. For simplicity, we assumed that the cross-spectral density between any two neurons is real-valued (i.e. all neurons are on average coherent at zero-phase). The power of the signal in the source (Area-1) equals

$$X_{\text{source,source}}(f) = N_t X(f) + N_t\,(N_t - 1)\,X(f)c(f)\,. \tag{30}$$

The power of the signal of the projection equals

$$X_{\text{proj,proj}}(f) = N_p X(f) + N_p\left(N_p - 1\right)X(f)c(f)\,. \tag{31}$$

The squared coherence now equals

$$C^2_{\text{proj,source}} \equiv \frac{|X_{\text{proj,source}}(f)|^2}{X_{\text{proj,proj}}(f)\,X_{\text{source,source}}(f)} = \cdots$$

$$\frac{\left(N_p X(f) + N_p\,(N_t - 1)\,X(f)c(f)\right)^2}{(N_t X(f) + N_t(N_t - 1)X(f)c(f))\;(N_p X(f) + N_p(N_p - 1)X(f)c(f))}\,, \tag{32}$$

which simplifies further to

$$C^2_{\text{proj,source}} = \frac{N_p\,(1 - c(f)) + c(f)N_p N_t}{N_t\,(1 - c(f)) + c(f)N_p N_t}\,. \tag{33}$$

Plugging in $g \equiv \frac{N_p}{N_t}$ where g is the fraction of projecting neurons, we obtain,

$$C^2_{\text{proj,source}} = \frac{c(f)g(N_t - 1) + g}{c(f)(gN_t - 1) + 1}\,. \tag{34}$$

By taking the Taylor expansion around $c(f) = 0$, since the coherence between two individual neurons will be small, we obtain the first-order approximation

$$\begin{aligned} C^2_{\text{proj,source}} &\approx g + c(f)(1 - g)gN_t \\ &\approx g + g\,c(f)\,N_t\,. \end{aligned} \tag{35}$$

Here we removed the term $(1-g)$ because we can assume that g is typically close to zero. Hence the projection-source coherence is proportional to the fraction of projecting neurons, plus the coherence times the total number of projecting neurons. We can furthermore relate $c(f)$ to the coherence of an individual neuron with the total signal in Area-1 (the spike field coherence). The squared-magnitude spike-field coherence can be expressed in terms of $c(f)$ as

$$\begin{aligned} \phi^2 &= \frac{((N_t - 1)\,c(f)X(f) + X(f))^2}{(N_t X(f) + (N_t - 1)\,N_t X(f)c(f))\,X(f)} \\ &= c(f)\left(1 - \frac{1}{N_t}\right) + \frac{1}{N_t}\,. \end{aligned} \tag{36}$$

Note that we used here

$$\begin{aligned} X_{\text{source},i} &= \sum_{j=1}^{N_t} X_{i,j} \\ &= X(f) + (N_t - 1)X(f)c(f) \end{aligned} \tag{37}$$

because we assumed all cross-spectra to be real-valued. Furthermore the total power in the source can be decomposed as

$$\begin{aligned} X_{\text{source,source}} &= \sum_{j=1}^{N_t}\sum_{i=1}^{N_t} X_{i,j} \\ &= N_t X(f) + N_t(N_t - 1)X(f)c(f)\,. \end{aligned} \tag{38}$$

bioRxiv preprint doi: https://doi.org/10.1101/2020.06.17.156190; this version posted June 18, 2020. The copyright holder for this preprint (which was not certified by peer review) is the author/funder. All rights reserved. No reuse allowed without permission.

Solving Eq. 36 for $c(f)$ yields

$$c(f) = \frac{\phi^2 N_t - 1}{N_t - 1}\,, \tag{39}$$

where $\phi^2 N_t \geq 1$. Plugging this into Eq. 35 we obtain the approximation

$$\begin{aligned} C^2_{\text{proj,source}} &\approx g + g\left(\phi^2 N_t - 1\right) \\ &\approx g\, N_t\, \phi^2\,. \end{aligned} \tag{40}$$

We thus obtain

$$C^2(f) \approx w^2(\alpha(f)+1)^2\phi^2\, g\, N_t\,. \tag{41}$$

Expression of the power on spike-field coherence.

We further expect $\alpha(f)$ to be proportional to ϕ^2: Let be $\phi(f)$ here is the consistency of single spikes (estimated by spike-field PPC) and divide the population into N_t spike trains of single spikes. The power due to the oscillation that is projected equals

$$\begin{aligned} S_{\text{osc}}(f) &= N_p X(f) + N_p(N_p-1)c(f)X(f) \\ &\approx N_p X(f) + N_p(N_p-1)\phi^2(f)X(f)\,. \end{aligned} \tag{42}$$

The power due to the background equals

$$\begin{aligned} S_{\text{background}}(f) &= N_p X(f) + N_p(N_p-1)c_{\text{background}}(f)X(f) \\ &\approx N_p X(f) + N_p(N_p-1)\phi^2_{\text{background}}(f)X(f)\,. \end{aligned} \tag{43}$$

Here $\phi_{\text{background}}$ is the spike-field coherence related to the background $1/f$ fluctuations, which may be non-zero. We note that if N_p is large enough, we have

$$\alpha(f) \to \frac{\phi^2(f)}{\phi^2_{\text{background}}}\,. \tag{44}$$

However, for small N_p, we obtain the first-order Taylor expansion

$$\alpha(f) \approx 1 + (N_p-1)\left(\phi^2(f) - \phi^2_{\text{background}}\right)\,. \tag{45}$$

In this case the SOS depends on N_p. The reason for that is that when N_p is small, the contribution of the phase consistency across neurons is relatively small and the intrinsic power due to the individual energy contributions weighs in.

Non-linear dependence of coherence on spike-field coherence and connection weight.

Because the connection weight w should be proportional to the total number of projection neurons (Markov et al., 2011), we therefore expect coherence to be proportional to w and ϕ. Combining all results we obtain:

$$C^2(f) \propto w^4\phi^4\,. \tag{46}$$

The factor ϕ^4 follows from the dependence of α on ϕ^2 and $C_{\text{proj,source}}(f)$ on ϕ^2. The factor w^4 follows from the dependence of $C^2(f)$ on w^2, the dependence of $\alpha(f)$ on N_p and therefore w, and the dependence of $C_{\text{proj,source}}(f)$ on N_p and therefore w. When the number of projection neurons N_p and $\phi(f)$ is sufficiently high, the projection-source coherence $C_{\text{proj,source}}(f)$ should converge to one, and $\alpha(f)$ to $\frac{\phi^2(f)}{\phi^2_{\text{background}}}$. In that regime we obtain

$$C^2(f) \propto w^2\phi^2\,. \tag{47}$$

bioRxiv preprint doi: https://doi.org/10.1101/2020.06.17.156190; this version posted June 18, 2020. The copyright holder for this preprint (which was not certified by peer review) is the author/funder. All rights reserved. No reuse allowed without permission.

Linear mixture with intrinsic noise in Area-1: simulations

For the purpose of simulations, we model the signal in Area-1 as follows:

$$z_1(t) \equiv s_1(t) + \sqrt{(1-\gamma)}\eta_1(t) + \sqrt{\gamma}\epsilon(t)\,. \tag{48}$$

The intrinsic signal $z_2(t)$ of Area-2 is defined as a linear mixture of its own background fluctuations, and the input from Area-1:

$$z_2(t) = \eta_2(t) + w(s_1(t) + \eta_1(t))\,. \tag{49}$$

For the purpose of simulations, we assume that the projected oscillatory component $s_1(t)$ is fully coherent with the oscillatory process in the sending area. We now obtain

$$\begin{aligned} Z_{12}(f) &= w(S_{11}(f) + \sqrt{(1-\gamma)}H(f)) \\ &= w(\alpha(f) + \sqrt{(1-\gamma)})H(f)\,. \end{aligned} \tag{50}$$

Since $\eta_1(t)$ and $\gamma_1(t)$ are uncorrelated:

$$\begin{aligned} Z_{11}(f) &= S_{11}(f) + (1-\gamma)H(f) + \gamma H(f) \\ &= S_{11}(f) + H(f) \\ &= (1+\alpha(f))H(f)\,; \end{aligned} \tag{51, 52}$$

$$\begin{aligned} Z_{22}(f) &= H(f) + w^2(S_{11}(f) + H(f)) \\ &= H(f) + w^2 Z_{11}(f) \\ &= (1 + w^2(1+\alpha))H(f)\,. \end{aligned} \tag{53}$$

The squared coherence $C_{12}(f)$ now simplifies as

$$C^2(f) = \frac{w^2(\alpha + \sqrt{(1-\gamma)})^2}{(1+\alpha(f))(1+w^2(1+\alpha(f)))}\,. \tag{54}$$

Plugging in $\alpha(f) = 0$ we obtain

$$C^2(f) = \frac{w^2(1-\gamma)}{(1+w^2)}\,. \tag{55}$$

This is comparable to Eq. 24.

Synthetic signals

Pink-noise signals

The background fluctuations in Figure 2 to 5 were simulated as $1/f^{2/3}$ pink-noise processes. For every trial we generate a trace of white noise sample points. Each traces was Fourier transformed. The complex coefficients of the positive frequencies were multiplied by the $1/f^{2/3}$-function. By concatenating the resulting coefficients with a flipped version of their complex conjugated we obtain a spectrum following the $1/f^{2/3}$-function. By inverse Fourier transforming the resulting spectrum we obtain a time series.

AR(2) model

The oscillatory processes in Figure 2 to 5 were simulated using an AR(2)-model. The AR(2)-model is defined as

$$x_t = a_1 x_{t-2} + a_2 x_{t-1} + \eta_t \tag{56}$$

where $\eta(t)$ is a white noise process with zero mean. To obtain a stationary signal, the roots must lie within the unit circle. If the AR process has complex conjugated roots it becomes a stochastic noise driven oscillator. The eigenvalues determine the strength of the oscillations.

bioRxiv preprint doi: https://doi.org/10.1101/2020.06.17.156190; this version posted June 18, 2020. The copyright holder for this preprint (which was not certified by peer review) is the author/funder. All rights reserved. No reuse allowed without permission.

Wilson-Cowan model

In this section we summarize the population model from Figure 4. The Wilson Cowan Model is a stochastic network model of nonlinear neuron models. It is often used to demonstrate the appearance of oscillations on a network scale (Powanwe and Longtin, 2019; Wallace et al., 2011; Wilson and Cowan, 1972). Each area shown in Figure 4 is modeled by a Wilson-Cowan model, composed of fully connected N_e excitatory and N_i inhibitory neurons. The neurons are modeled as two-state Markov processes (one active and one quiescent state). The transition probability of neuron i to change from the active to the quiescent state equals:

$$P_i(active \rightarrow quiescent, dt) = \alpha_i dt\,. \tag{57}$$

Whereas the transition probability of neuron i to change from the quiescent to the active state is as follows:

$$P_i(quiescent \rightarrow active, dt) = \beta_i f_i\left(s_i(t)\right) dt\,. \tag{58}$$

Here the activation function is defined:

$$f(s) \equiv \frac{1}{1+e^{-s}} \tag{59}$$

The total input current s_E to excitatory neurons and s_I to inhibitory neurons is given by:

$$s_E(t) = \frac{W_{ee}}{N_e}k(t) - \frac{W_{ei}}{N_I}l(t) + h_E \tag{60}$$

and

$$s_I(t) = \frac{W_{ie}}{N_e}k(t) - \frac{W_{ii}}{N_I}l(t) + h_I\,, \tag{61}$$

where h_I and h_E are the external input current to the correspondent neuron types. The number of active excitatory neurons is referred to as $k(t)$ and the number of active inhibitory neurons as $l(t)$. The synaptic strength from excitatory neurons to inhibitory neurons is W_{ie}, accordingly W_{ei} is the synaptic strength from inhibitory neurons to excitatory neurons. The total synaptic weight between excitatory neurons is referred to as W_{ee}, whereas the total synaptic weight between excitatory neurons is referred to as W_{ii}.

The model determines the rates of transition between states by the variables alpha and beta. However, since biological networks are stochastic processes, it is necessary to randomize the time of the next event. We achieved this by running the simulation with a Gillespie algorithm (Gillespie, 1977). In the scenario of "synaptic mixing with entrainment", the excitatory neurons from Area-1 formed connections with the excitatory neurons of Area-2. This changes equation 60 for region 2 as follows:

$$s_{E,2}(t) = \frac{W_{ee,2}}{N_{e,2}}k_2(t) - \frac{W_{ei,2}}{N_{I,2}}l_2(t) + \frac{W_{ee,1}}{N_{e,1}}k_1(t) + h_{E,2}\,. \tag{62}$$

Whereas the neurons within an area are all-to-all connected, the inter-regional connection rate in 6 B to D (right) is 5%. For simplification, each connection is represented in the LFP signal as one synapse. We calculated the LFP signal by convolving every incoming spike to an area with an alpha function $\alpha(t) \equiv g(e^{-t/\tau_1} - e^{-t/\tau_2})$. The variable t is defined as the time relative to the spike onset and $\alpha(t) = 0$ for $t < 0$. The factor g is defined as $g = -1$ for inhibitory synapses and $g = 1$ for excitatory synapses. Finally, the synaptic potentials of all input connections within an area are summed up to calculate an overall LFP signal of the corresponding area.

Each simulated area consists of 800 excitatory and 200 inhibitory neurons. The neurons within one area are fully connected. In Figure 6 A-D, each neuron in Area-2 received inputs from 40 randomly chosen excitatory neurons within Area-1. All simulations in Figure 6 have the following parameter values, $W_{ee} = 25.4$, $W_{ii} = 1.3$, $W_{ei} = 24.3$, $W_{ie} = 30$, $h_E = -3.8$, $h_I = -3.8$. Areas oscillating in the beta-frequency band have parameter values $\alpha_e = 0.038$, $\alpha_i = 0.076$, $\beta_e = 0.379$ $\beta_i = 0.758$. Areas oscillating in the gamma-frequency band have parameter values $\alpha_e = 0.1$, $\alpha_i = 0.2$, $\beta_e = 1$ $\beta_i = 2$.

bioRxiv preprint doi: https://doi.org/10.1101/2020.06.17.156190; this version posted June 18, 2020. The copyright holder for this preprint (which was not certified by peer review) is the author/funder. All rights reserved. No reuse allowed without permission.

Extension to spiking activity

The same model developed for field-field coherence should apply to spiking activity, if spiking relates in a linear or sigmoidal way to synaptic inputs. Consider that $z_2(t)$ represents the average voltage fluctuations in the receiver. If population spiking activity is a linear function of $z_2(t)$, i.e. $y_2(t) = z_2(t)$, then the same equation for coherence applies. Because spiking activity is stochastic and sparse for a single neuron, a population of neurons will contain additional variance that suppresses the coherence, i.e. we can write

$$y_2(t) = s_2(t) + \xi_2(t) + w\left(s_1^*(t) + \epsilon_1(t)\right) . \tag{63}$$

where $s_2(t)$ is the intrinsic signal in the receiver. This distortion ξ_2, which should decrease with the number of neurons, will decrease the interareal spike-field coherence by increasing the intrinsic power in the receiver. Next, consider the case where the population spiking activity is a standard sigmoidal activation function of $z_2(t)$, i.e.

$$y_2(t) = \sigma(z_2(t)) , \tag{64}$$

where $\sigma(x) \equiv 1/(1 + \exp(-x))$. In analogy to the data processing equality, we expect that the coherence after the transformation should always be lower than in the linear case, because the signal gets distorted by the sigmoid transformation, and coherence expresses the amount of variance that can be explained by linear prediction. Assuming that w is relatively small we can make a Taylor-expansion around $w = 0$ and obtain

$$y_2(t) = \sigma(s_2(t) + \xi_2(t)) + w\, s_1^*(t)\, \dot{\sigma}(s_2(t) + \xi_2(t)) ,$$

where $\dot{\sigma}(x)$ denotes the first derivative of the sigmoid function at x. Note that

$$\begin{aligned} &\mathrm{E}\left\{s_1^*(t) s_1^*(t+\tau)\, \dot{\sigma}(s_2(t+\tau) + \xi_2(t+\tau))\right\} \\ &= \mathrm{E}\{s_1^*(t) s_1^*(t+\tau)\}\, \mathrm{E}\{\dot{\sigma}(s_2(t+\tau) + \xi_2(t+\tau))\} . \end{aligned} \tag{65}$$

We can thus scale the signal as follows. Define a new transformation function by scaling inside the sigmoid as

$$v(x) = \sigma\left(\frac{x}{\mathrm{E}\{\dot{\sigma}(x)\}}\right) . \tag{66}$$

Assuming that $s_1(t)$ and $s_2(t)$ are statistically independent, we can see that the resulting coherence between $z_1(t)$ and $y_2(t)$ now equals

$$C^2_{\text{Area-1-LFP, Area-2-Spikes}} \approx \frac{C^2_{\text{proj,source}} w^2}{\dfrac{S^v_{22}(f)}{S_{11}(f)} + w^2} . \tag{67}$$

where $S^v_{22}(f)$ is the spectral density function of $v(s_2(t) + \xi_2(t))$. Here, we can recognize that the equation has the same form above and is scaled by the weight and the projection-source coherence; for small w this dependence is linear. To conclude, in case of a sigmoid input-output curve:

1. For small w, the squared spike-field coherence scales with w^2 and $C^2_{\text{proj,source}}$, similar to the case of field-field coherence.
2. Coherence between Area-1 LFP and a population of spikes in Area-2 will be lower compared to field-field coherence because the spikes will be a noisy approximation of the input signal (for a finite population). Suppose that $y_2(t)$ reflects the superposition of spiking traces from a population of neurons. The number of neurons that we superimpose in the receiver has two effects: (i) If we assume that each neuron receives the same input, then adding more neurons increases the coherence between the Area-1 LFP and the Area-2 spikes, because the population sum becomes a more accurate approximation of the LFP (Zeitler et al., 2006; Vinck et al., 2012) (i.e. in the equation above, $\xi(t)$ will decrease). (ii) Each neuron the receiver may receive synaptic inputs from only a few Area-1 projection neurons. That is, the number of projection neurons sending inputs to a single neuron in the receiver will now be equal to $N_p k$, where k is the fraction of projection neurons that goes to a single neuron in the receiver. Therefore, $C^2_{\text{proj,source}}$ may be very small for a single neuron, and it should increase with number of neurons we superimpose. Thus, the coherence between the sum of a population of Area-2 neurons and the Area-1 LFP should depend in a non-linear way on the number of neurons we sum over.

bioRxiv preprint doi: https://doi.org/10.1101/2020.06.17.156190; this version posted June 18, 2020. The copyright holder for this preprint (which was not certified by peer review) is the author/funder. All rights reserved. No reuse allowed without permission.

3. We expect that if the spikes are a non-linear function of the input signal, there will be a frequency-dependent distortion in interareal coherence; we expect this always to be a reduction, which remains to be proven. The distortion might be greater at higher frequencies, because the sigmoid transformation of low-frequency fluctuations can increase energy at high frequencies.

References

Abeles, M., 1982. Role of the cortical neuron: integrator or coincidence detector? Isr. Med. Assoc. J 18, 83.

Akam, T.E., Kullmann, D.M., 2012. Efficient "Communication through Coherence" Requires Oscillations Structured to Minimize Interference between Signals. PLOS Comp. Biol. 8, e1002760.

Babapoor-Farrokhran, S., Vinck, M., Womelsdorf, T., Everling, S., 2017. Theta and beta synchrony coordinate frontal eye fields and anterior cingulate cortex during sensorimotor mapping. Nature Communications , 13967.

Bastos, A.M., Vezoli, J., Bosman, C.A., Schoffelen, J.M., Oostenveld, R., Dowdall, J.R., De Weerd, P., Kennedy, H., Fries, P., 2015. Visual areas exert feedforward and feedback influences through distinct frequency channels. Neuron 85, 390–401.

Batista-Brito, R., Zagha, E., Ratliff, J.M., Vinck, M., 2018. Modulation of cortical circuits by top-down processing and arousal state in health and disease. Current opinion in neurobiology 52, 172–181.

Bonnefond, M., Kastner, S., Jensen, O., 2017. Communication between brain areas based on nested oscillations. eneuro 4.

Börgers, C., Kopell, N.J., 2008. Gamma oscillations and stimulus selection. Neural Comput 20, 383–414.

Bosman, C., Schoffelen, J., Brunet, N., Oostenveld, R., Bastos, A., Womelsdorf, T., Rubehn, B., Stieglitz, T., De Weerd, P., Fries, P., 2012. Attentional stimulus selection through selective synchronization between monkey visual areas. Neuron 75, 875–888.

Bragin, A., Jandó, G., Nádasdy, Z., Hetke, J., Wise, K., Buzsáki, G., 1995. Gamma (40-100 hz) oscillation in the hippocampus of the behaving rat. J Neurosci 15, 47–60.

Bressler, S.L., 1995. Large-scale cortical networks and cognition. Brain Research Reviews 20, 288–304.

Bressler, S.L., Coppola, R., Nakamura, R., 1993. Episodic multiregional cortical coherence at multiple frequencies during visual task performance. Nature 366, 153–156.

Bressler, S.L., Richter, C.G., Chen, Y., Ding, M., 2006. Top-down cortical influences in visual expectation, in: IJCNN'06., pp. 188–194.

Brovelli, A., Ding, M., Ledberg, A., Chen, Y., Nakamura, R., Bressler, S.L., 2004. Beta oscillations in a large-scale sensorimotor cortical network: directional influences revealed by granger causality. Proc. Natl. Acad. Sci. U.S.A. 101, 9849–9854.

Brunet, N.M., Bosman, C.A., Vinck, M., Roberts, M., Oostenveld, R., Desimone, R., De Weerd, P., Fries, P., 2014. Stimulus repetition modulates gamma-band synchronization in primate visual cortex. Proc. Natl. Acad. Sci. U.S.A. 111, 3626–3631.

Buffalo, E.A., Fries, P., Landman, R., Buschman, T.J., Desimone, R., 2011. Laminar differences in gamma and alpha coherence in the ventral stream. Proc. Natl. Acad. Sci. U.S.A. 108, 11262–11267.

Burchell, T.R., Faulkner, H.J., Whittington, M.A., 1998. Gamma frequency oscillations gate temporally coded afferent inputs in the rat hippocampal slice. Neurosci Lett 255, 151–4.

Burns, S.P., Xing, D., Shapley, R.M., 2011. Is gamma-band activity in the local field potential of V1 cortex a "clock" or filtered noise? J. Neurosci. 31, 9658–9664.

Buschman, T.J., Miller, E.K., 2007. Top-down versus bottom-up control of attention in the prefrontal and posterior parietal cortices. Science 315, 1860–2.

Buzsáki, G., 2006. Rhythms of the Brain. Oxford University Press, USA.

Buzsáki, G., Anastassiou, C.A., Koch, C., 2012. The origin of extracellular fields and currents–EEG, ECoG, LFP and spikes. Nat. Rev. Neurosci. 13, 407–420.

Buzsáki, G., Draguhn, A., 2004. Neuronal oscillations in cortical networks. Science 304, 1926–1929.

Buzsáki, G., Schomburg, E.W., 2015. What does gamma coherence tell us about inter-regional neural communication? Nature neuroscience 18, 484–489.

Carmichael, J.E., Yuen, M.M., Van Der Meer, M.A., 2019. Piriform cortex provides a dominant gamma lfp oscillation in the anterior limbic system. BioRxiv , 861021.

Chalk, M., Herrero, J.L., Gieselmann, M.A., Delicato, L.S., Gotthardt, S., Thiele, A., 2010. Attention reduces stimulus-driven gamma frequency oscillations and spike field coherence in V1. Neuron 66, 114–25.

Chiu, C.Q., Lur, G., Morse, T.M., Carnevale, N.T., Ellis-Davies, G.C., Higley, M.J., 2013. Compartmentalization of gabaergic inhibition by dendritic spines. Science 340, 759–762.

Christensen, J.R., Larsen, K.B., Lisanby, S.H., Scalia, J., Arango, V., Dwork, A.J., Pakkenberg, B., 2007. Neocortical and hippocampal neuron and glial cell numbers in the rhesus monkey. The Anatomical Record: Advances in Integrative Anatomy and Evolutionary Biology: Advances in Integrative Anatomy and Evolutionary Biology 290, 330–340.

Colgin, L., Denninger, T., Fyhn, M., Hafting, T., Bonnevie, T., Jensen, O., Moser, M., Moser, E., 2009. Frequency of gamma oscillations routes flow of information in the hippocampus. Nature 462, 353–357.

Dann, B., Michaels, J.A., Schaffelhofer, S., Scherberger, H., 2016. Uniting functional network topology and oscillations in the fronto-parietal single unit network of behaving primates. Elife 5, e15719.

Donoghue, J.P., Sanes, J.N., Hatsopoulos, N.G., Gaal, G., 1998. Neural discharge and local field potential oscillations in primate motor cortex during voluntary movements. J Neurophysiol 79, 159–173.

Einevoll, G.T., Kayser, C., Logothetis, N.K., Panzeri, S., 2013. Modelling and analysis of local field potentials for studying the function of cortical circuits. Nat. Rev. Neurosci. 14, 770–785.

Engel, A.K., Fries, P., Singer, W., 2001. Dynamic predictions: oscillations and synchrony in top-down processing. Nat. Rev. Neurosci. 2, 704–716.

Ferro, D., van Kempen, J., Boyd, M., Panzeri, S., Thiele, A., 2020. Directed information exchange between cortical layers in macaque v1 and v4 and its modulation by selective attention. bioRxiv .

bioRxiv preprint doi: https://doi.org/10.1101/2020.06.17.156190; this version posted June 18, 2020. The copyright holder for this preprint (which was not certified by peer review) is the author/funder. All rights reserved. No reuse allowed without permission.

Fries, P., 2005. A mechanism for cognitive dynamics: neuronal communication through neuronal coherence. Trends Cogn. Sci. 9, 474–480.
Fries, P., 2009. Neuronal gamma-band synchronization as a fundamental process in cortical computation. Annu. Rev. Neurosci. 32, 209–224.
Fries, P., 2015. Rhythm for Cognition: Communication Through Coherence. Neuron 88, 220–235. arXiv:15334406.
Geweke, J., 1982. Measurement of linear dependence and feedback between multiple time series. Journal of the American Statistical Association 77, 304–313.
Gillespie, D.T., 1977. Exact stochastic simulation of coupled chemical reactions. The journal of physical chemistry 81, 2340–2361.
Gray, C., McCormick, D., 1996. Chattering cells: superficial pyramidal neurons contributing to the generation of synchronous oscillations in the visual cortex. Science 274, 109.
Gray, C.M., König, P., Engel, A.K., Singer, W., 1989. Oscillatory responses in cat visual cortex exhibit inter-columnar synchronization which reflects global stimulus properties. Nature 338, 334–337.
Gregoriou, G.G., Gotts, S.J., Zhou, H., Desimone, R., 2009. High-frequency, long-range coupling between prefrontal and visual cortex during attention. Science 324, 1207–1210.
Grothe, I., Neitzel, S.D., Mandon, S., Kreiter, A.K., 2012a. Switching neuronal inputs by differential modulations of gamma-band phase-coherence. J. Neurosci. 32, 16172–16180.
Grothe, I., Neitzel, S.D., Mandon, S., Kreiter, A.K., 2012b. Switching Neuronal Inputs by Differential Modulations of Gamma-Band Phase-Coherence. J. Neurosci. 32, 16172–16180.
Hagan, M.A., Dean, H.L., Pesaran, B., 2012. Spike-field activity in parietal area lip during coordinated reach and saccade movements. Journal of neurophysiology 107, 1275–1290.
Han, Y., Kebschull, J.M., Campbell, R.A., Cowan, D., Imhof, F., Zador, A.M., Mrsic-Flogel, T.D., 2018. The logic of single-cell projections from visual cortex. Nature 556, 51–56.
Haufe, S., Nikulin, V.V., Nolte, G., 2012. Alleviating the influence of weak data asymmetries on granger-causal analyses, in: Latent Variable Analysis and Signal Separation. Springer, pp. 25–33.
Henrie, J.A., Shapley, R., 2005. LFP Power Spectra in V1 Cortex: The Graded Effect of Stimulus Contrast. J. Neurophysiol. 94, 479–490.
Hermes, D., Miller, K., Wandell, B., Winawer, J., 2015. Stimulus Dependence of Gamma Oscillations in Human Visual Cortex. Cereb. Cortex. 25, 2951–2959.
Johnson, P.B., Ferraina, S., Bianchi, L., Caminiti, R., 1996. Cortical networks for visual reaching: physiological and anatomical organization of frontal and parietal lobe arm regions. Cerebral cortex 6, 102–119.
Katzner, S., Nauhaus, I., Benucci, A., Bonin, V., Ringach, D.L., Carandini, M., 2009. Local origin of field potentials in visual cortex. Neuron 61, 35–41.
van Kerkoerle, T., Self, M.W., Dagnino, B., Gariel-Mathis, M.A., Poort, J., van der Togt, C., Roelfsema, P.R., 2014. Alpha and gamma oscillations characterize feedback and feedforward processing in monkey visual cortex. Proc. Natl. Acad. Sci. U.S.A. , 201402773.
Kreiter, A.K., 2006. How do we model attention-dependent signal routing? Neural networks 19, 1443–1444.
Lindén, H., Tetzlaff, T., Potjans, T.C., Pettersen, K.H., Grün, S., Diesmann, M., Einevoll, G.T., 2011. Modeling the Spatial Reach of the LFP. Neuron 72, 859–872.
Livingstone, M.S., 1996. Oscillatory firing and interneuronal correlations in squirrel monkey striate cortex. J. Neurophysiol. 75, 2467–2485.
Luck, S.J., Chelazzi, L., Hillyard, S.A., Desimone, R., 1997. Neural mechanisms of spatial selective attention in areas v1, v2, and v4 of macaque visual cortex. Journal of neurophysiology 77, 24–42.
Lund, J.S., Angelucci, A., Bressloff, P.C., 2003. Anatomical substrates for functional columns in macaque monkey primary visual cortex. Cereb. Cortex. 13, 15–24.
Luppino, G., Murata, A., Govoni, P., Matelli, M., 1999. Largely segregated parietofrontal connections linking rostral intraparietal cortex (areas aip and vip) and the ventral premotor cortex (areas f5 and f4). Experimental Brain Research 128, 181–187.
Lur, G., Vinck, M.A., Tang, L., Cardin, J.A., Higley, M.J., 2016. Projection-Specific Visual Feature Encoding by Layer 5 Cortical Subnetworks. Cell Reports 14, 2538–2545.
Markov, N., Misery, P., Falchier, A., Lamy, C., Vezoli, J., Quilodran, R., Gariel, M., Giroud, P., Ercsey-Ravasz, M., Pilaz, L., et al., 2011. Weight consistency specifies regularities of macaque cortical networks. Cerebral cortex 21, 1254–1272.
Markov, N.T., Vezoli, J., Chameau, P., Falchier, A., Quilodran, R., Huissoud, C., Lamy, C., Misery, P., Giroud, P., Ullman, S., et al., 2014. Anatomy of hierarchy: Feedforward and feedback pathways in macaque visual cortex. Journal of Comparative Neurology 522, 225–259.
McGinley, M.J., Vinck, M., Reimer, J., Batista-Brito, R., Zagha, E., Cadwell, C.R., Tolias, A.S., Cardin, J.A., McCormick, D.A., 2015. Waking State: Rapid Variations Modulate Neural and Behavioral Responses. Neuron 87, 1143–1161.
Mejias, J.F., Murray, J.D., Kennedy, H., Wang, X.J., 2016. Feedforward and feedback frequency-dependent interactions in a large-scale laminar network of the primate cortex. Science advances 2, e1601335.
Michalareas, G., Vezoli, J., van Pelt, S., Schoffelen, J.M., Kennedy, H., Fries, P., 2016. Alpha-Beta and Gamma Rhythms Subserve Feedback and Feedforward Influences among Human Visual Cortical Areas. Neuron 89, 384–397. arXiv:15334406.
Miller, E.K., Wilson, M.A., 2008. All my circuits: using multiple electrodes to understand functioning neural networks. Neuron 60, 483–8.
Mitzdorf, U., 1985. Current source-density method and application in cat cerebral cortex: investigation of evoked potentials and EEG phenomena. Physiol. Rev. 65, 37–100.
Montgomery, S.M., Buzsáki, G., 2007. Gamma oscillations dynamically couple hippocampal ca3 and ca1 regions during memory task performance. Proc. Natl. Acad. Sci. U.S.A. 104, 14495–14500.
Murray, J.D., Bernacchia, A., Freedman, D.J., Romo, R., Wallis, J.D., Cai, X., Padoa-Schioppa, C., Pasternak, T., Seo, H., Lee, D., et al., 2014. A hierarchy of intrinsic timescales across primate cortex. Nature neuroscience 17, 1661.
Murthy, V.N., Fetz, E.E., 1996. Oscillatory activity in sensorimotor cortex of awake monkeys: synchronization of local field potentials and relation to behavior. J. Neurophysiol. 76, 3949–3967.
Nicolelis, M.A., Baccala, L.A., Lin, R., Chapin, J.K., 1995. Sensorimotor encoding by synchronous neural ensemble activity at multiple levels of the somatosensory system. Science 268, 1353–1358.
Nolte, G., Bai, O., Wheaton, L., Mari, Z., Vorbach, S., Hallett, M., 2004. Identifying true brain interaction from EEG data using the imaginary part

bioRxiv preprint doi: https://doi.org/10.1101/2020.06.17.156190; this version posted June 18, 2020. The copyright holder for this preprint (which was not certified by peer review) is the author/funder. All rights reserved. No reuse allowed without permission.

of coherency. Clin Neurophysiol 115, 2292–2307.

Nunez, P.L., Srinivasan, R., 2006. Electric fields of the brain: the neurophysics of EEG? Oxford University Press.

Olcese, U., Bos, J.J., Vinck, M., Lankelma, J.V., van Mourik-Donga, L.B., Schlumm, F., Pennartz, C.M., 2016. Spike-based functional connectivity in cerebral cortex and hippocampus: loss of global connectivity is coupled to preservation of local connectivity during non-rem sleep. Journal of Neuroscience 36, 7676–7692.

Onorato, I., Neuenschwander, S., Hoy, J., Lima, B., Rocha, K.S., Broggini, A.C., Uran, C., Spyropoulos, G., Klon-Lipok, J., Womelsdorf, T., Fries, P., Niell, C., Singer, W., Vinck, M., 2020. A distinct class of bursting neurons with strong gamma synchronization and stimulus selectivity in monkey v1. Neuron 105, 180–197.

Oostenveld, R., Fries, P., Maris, E., Schoffelen, J.M., 2011. FieldTrip: Open source software for advanced analysis of MEG, EEG, and invasive electrophysiological data. Comput Intell Neurosci 2011, 156869.

Palmigiano, A., Geisel, T., Wolf, F., Battaglia, D., 2017. Flexible information routing by transient synchrony. Nature neuroscience 20, 1014.

Parabucki, A., Lampl, I., 2017. Volume conduction coupling of whisker-evoked cortical lfp in the mouse olfactory bulb. Cell reports 21, 919–925.

Pesaran, B., Vinck, M., Einevoll, G., Sirota, A., Fries, P., Siegel, M., Truccolo, W., Schroeder, C., Srinivasan, R., 2018. Investigating large-scale brain dynamics using field potential recordings: analysis and interpretation. Nat. Neurosci. .

Peter, A., Uran, C., Klon-Lipok, J., Roese, R., Van Stijn, S., Barnes, W., Dowdall, J.R., Singer, W., Fries, P., Vinck, M., 2019. Surface color and predictability determine contextual modulation of v1 firing and gamma oscillations. eLife 8, e42101.

Phillips, J.M., Vinck, M., Everling, S., Womelsdorf, T., 2014. A long-range fronto-parietal 5-to 10-hz network predicts "top-down" controlled guidance in a task-switch paradigm. Cerebral Cortex 24, 1996–2008.

Pike, F., Goddard, R., Suckling, J., Ganter, P., Kasthuri, N., Paulsen, O., 2000. Distinct frequency preferences of different types of rat hippocampal neurones in response to oscillatory input currents. The Journal of Physiology 529, 205.

Powanwe, A.S., Longtin, A., 2019. Determinants of brain rhythm burst statistics. Scientific Reports 9, 1–23.

Ray, S., Maunsell, J.H., 2015. Do gamma oscillations play a role in cerebral cortex? Trends in cognitive sciences 19, 78–85.

Richter, C.G., Coppola, R., Bressler, S.L., 2018. Top-down beta oscillatory signaling conveys behavioral context in early visual cortex. Sci. Rep. 8, 6991.

Salazar, R., Dotson, N., Bressler, S., Gray, C., 2012a. Content-specific fronto-parietal synchronization during visual working memory. Science 338, 1097–1100.

Salazar, R.F., Dotson, N.M., Bressler, S.L., Gray, C.M., 2012b. Content-Specific Fronto-Parietal Synchronization During Visual Working Memory. Science 338, 1097–1100.

Saleem, A.B., Lien, A.D., Krumin, M., Haider, B., Rosón, M.R., Ayaz, A., Reinhold, K., Busse, L., Carandini, M., Harris, K.D., 2017. Subcortical Source and Modulation of the Narrowband Gamma Oscillation in Mouse Visual Cortex. Neuron 93, 315–322.

Salinas, E., Sejnowski, T.J., 2001. Correlated neuronal activity and the flow of neural information. Nat Rev Neurosci 2, 539–50.

Scherberger, H., Jarvis, M.R., Andersen, R.A., 2005. Cortical local field potential encodes movement intentions in the posterior parietal cortex. Neuron 46, 347–354.

Schomburg, E.W., Fernández-Ruiz, A., Mizuseki, K., Berényi, A., Anastassiou, C.A., Koch, C., Buzsáki, G., 2014. Theta phase segregation of input-specific gamma patterns in entorhinal-hippocampal networks. Neuron 84, 470–485.

Siegle, J.H., Jia, X., Durand, S., Gale, S., Bennett, C., Graddis, N., Heller, G., Ramirez, T.K., Choi, H., Luviano, J.A., et al., 2019. A survey of spiking activity reveals a functional hierarchy of mouse corticothalamic visual areas. bioRxiv , 805010.

Singer, W., Gray, C.M., 1995. Visual feature integration and the temporal correlation hypothesis. Annu. Rev. Neurosci. 18, 555–586.

Sirota, A., Montgomery, S., Fujisawa, S., Isomura, Y., Zugaro, M., Buzsáki, G., 2008a. Entrainment of neocortical neurons and gamma oscillations by the hippocampal theta rhythm. Neuron 60, 683–697.

Sirota, A., Montgomery, S., Fujisawa, S., Isomura, Y., Zugaro, M., Buzsáki, G., 2008b. Entrainment of Neocortical Neurons and Gamma Oscillations by the Hippocampal Theta Rhythm. Neuron 60, 683–697.

Spyropoulos, G., Dowdall, J.R., Schölvinck, M.L., Bosman, C.A., Lima, B., Peter, A., Onorato, I., Klon-Lipok, J., Roese, R., Neuenschwander, S., Wolf, S., Vinck, M., Fries, P., 2020. Spontaneous variability in gamma dynamics described by a linear harmonic oscillator driven by noise. bioRxiv , 793729.

Steriade, M., McCormick, D.A., Sejnowski, T.J., 1993. Thalamocortical oscillations in the sleeping and aroused brain. Science 262, 679–685.

Tiesinga, P., Sejnowski, T., 2010. Mechanisms for phase shifting in cortical networks and their role in communication through coherence. Front. Hum. Neurosci 4.

Trongnetrpunya, A., Nandi, B., Kang, D., Kocsis, B., Schroeder, C.E., Ding, M., 2016. Assessing granger causality in electrophysiological data: removing the adverse effects of common signals via bipolar derivations. Frontiers in systems neuroscience 9, 189.

Varela, F., Lachaux, J.P., Rodriguez, E., Martinerie, J., 2001. The brainweb: phase synchronization and large-scale integration. Nat. Rev. Neurosci. 2, 229–239.

Vinck, M., Battaglia, F.P., Womelsdorf, T., Pennartz, C., 2012. Improved measures of phase-coupling between spikes and the Local Field Potential. J Comput Neurosci 33, 53–75.

Vinck, M., Bos, J.J., Mourik-Donga, V., Laura, A., Oplaat, K.T., Klein, G.A., Jackson, J.C., Gentet, L.J., Pennartz, C., 2016. Cell-type and state-dependent synchronization among rodent somatosensory, visual, perirhinal cortex, and hippocampus ca1. Frontiers in systems neuroscience 9, 187.

Vinck, M., Bosman, C.A., 2016. More gamma more predictions: Gamma-synchronization as a key mechanism for efficient integration of classical receptive field inputs with surround predictions. Front Syst Neurosci 10, 35.

Vinck, M., Huurdeman, L., Bosman, C.A., Fries, P., Battaglia, F.P., Pennartz, C.M., Tiesinga, P.H., 2015. How to detect the granger-causal flow direction in the presence of additive noise? Neuroimage 108, 301–318.

Vinck, M., Oostenveld, R., van Wingerden, M., Battaglia, F., Pennartz, C.M., 2011. An improved index of phase-synchronization for electrophysiological data in the presence of volume-conduction, noise and sample-size bias. Neuroimage 55, 1548–1565.

Vinck, M., van Wingerden, M., Womelsdorf, T., Fries, P., Pennartz, C.M., 2010. The pairwise phase consistency: a bias-free measure of rhythmic neuronal synchronization. Neuroimage 51, 112–122.

bioRxiv preprint doi: https://doi.org/10.1101/2020.06.17.156190; this version posted June 18, 2020. The copyright holder for this preprint (which was not certified by peer review) is the author/funder. All rights reserved. No reuse allowed without permission.

Vinck, M., Womelsdorf, T., Buffalo, E.A., Desimone, R., Fries, P., 2013a. Attentional modulation of cell-class-specific gamma-band synchronization in awake monkey area V4. Neuron 80, 1077–1089.

Vinck, M., Womelsdorf, T., Fries, P., 2013b. Gamma-band synchronization and information transmission, in: Quiroga-Quian, R., Panzeri, S. (Eds.), Principles of Neural Coding. CRC Press.

Volgushev, M., Chistiakova, M., Singer, W., 1998. Modification of discharge patterns of neocortical neurons by induced oscillations of the membrane potential. Neuroscience 83, 15–25.

Von Stein, A., Sarnthein, J., 2000. Different frequencies for different scales of cortical integration: from local gamma to long range alpha/theta synchronization. International Journal of Psychophysiology 38, 301–313.

Wallace, E., Benayoun, M., Van Drongelen, W., Cowan, J.D., 2011. Emergent oscillations in networks of stochastic spiking neurons. Plos one 6.

Wang, X.J., 2002. Pacemaker neurons for the theta rhythm and their synchronization in the septohippocampal reciprocal loop. Journal of neurophysiology 87, 889–900.

Wilson, H.R., Cowan, J.D., 1972. Excitatory and inhibitory interactions in localized populations of model neurons. Biophys. J. 12, 1–24.

Xing, D., Yeh, C.I., Burns, S., Shapley, R.M., 2012. Laminar analysis of visually evoked activity in the primary visual cortex. Proc. Natl. Acad. Sci. U.S.A. 109, 13871–13876.

Zeitler, M., Fries, P., Gielen, S., 2006. Assessing neuronal coherence with single-unit, multi-unit, and local field potentials. Neural Comput 18, 2256–2281.